Article

Cancer Cell

The Link between the Multiverse of Immune Microenvironments in Metastases and the Survival of Colorectal Cancer Patients

Graphical Abstract

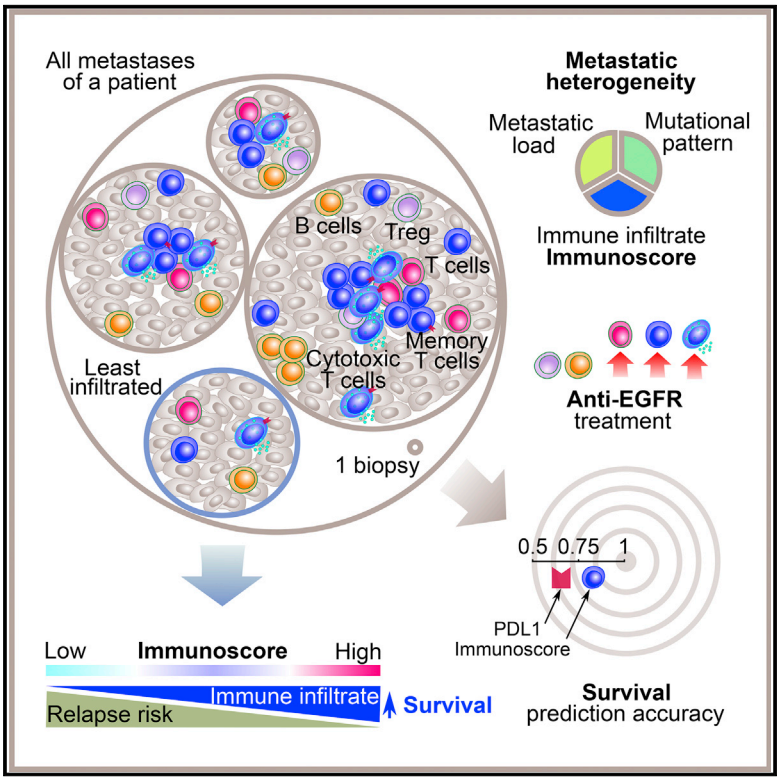

Highlights

- Inter- and intra-metastatic immune infiltrates are heterogeneous in colorectal cancer
- T cell densities from metastases increase following anti-EGFR treatment
- Immunoscore (IS) outperforms PDL1 staining in metastatic biopsy diagnostic accuracy
- IS and TB score from the least-infiltrated metastasis are most survival associated

Authors

Marc Van den Eynde, Bernhard Mlecnik, Gabriela Bindea, ..., Franck Pagès, Jean-Pascal Machiels, Jérôme Galon

Correspondence

jerome.galon@crc.jussieu.fr

In Brief

Van den Eynde et al. quantify immune cell types in metastases and primary colorectal tumors. They show that high Immunoscore (IS) associates with fewer metastases, that anti-EGFR treatment significantly increases T cell density in the core of metastases, and that the predictive accuracy of IS better than PDL1.

Van den Eynde et al., 2018, Cancer Cell *34*, 1012–1026
December 10, 2018
https://doi.org/10.1016/j.ccell.2018.11.003

CellPress

CellPress

Cancer Cell
Article

The Link between the Multiverse of Immune Microenvironments in Metastases and the Survival of Colorectal Cancer Patients

Marc Van den Eynde,[1,2,9] Bernhard Mlecnik,[2,3,9] Gabriela Bindea,[2,9] Tessa Fredriksen,[2] Sarah E. Church,[2] Lucie Lafontaine,[2] Nacilla Haicheur,[4] Florence Marliot,[2,4] Mihaela Angelova,[2] Angela Vasaturo,[2] Daniela Bruni,[2] Anne Jouret-Mourin,[1] Pamela Baldin,[1] Nicolas Huyghe,[1] Karin Haustermans,[5,6] Annelies Debucquoy,[5] Eric Van Cutsem,[7] Jean-Francois Gigot,[1] Catherine Hubert,[1] Alex Kartheuser,[1] Christophe Remue,[1] Daniel Léonard,[1] Viia Valge-Archer,[8] Franck Pagès,[2,4] Jean-Pascal Machiels,[1] and Jérôme Galon[2,10,*]

[1]Institut Roi Albert II, Department of Medical Oncology Cliniques Universitaires St-Luc and Institut de Recherche Clinique et Experimentale (Pole MIRO), Université Catholique de Louvain, 1200 Brussels, Belgium
[2]INSERM, Laboratory of Integrative Cancer Immunology, Sorbonne Université, Sorbonne Paris Cité, Université Paris Descartes, Université Paris Diderot; Centre de Recherche des Cordeliers, 75006 Paris, France
[3]Inovarion, 75013 Paris, France
[4]AP-HP, Assistance Publique-Hopitaux de Paris, Departments of Immunology, HEGP, 75015 Paris, France
[5]Laboratory of Experimental Radiotherapy, Department of Oncology, KU Leuven, 3000 Leuven, Belgium
[6]University Hospitals Leuven, Department of Radiation Oncology, 3000 Leuven, Belgium
[7]University Hospitals Leuven, Department of Gastroenterology, 3000 Leuven, Belgium
[8]AstraZeneca, Cambridge CB2 0AA, UK
[9]These authors contributed equally
[10]Lead Contact
*Correspondence: jerome.galon@crc.jussieu.fr
https://doi.org/10.1016/j.ccell.2018.11.003

SUMMARY

Treatment of metastatic colorectal cancer is based upon the assumption that metastases are homogeneous within a patient. We quantified immune cell types of 603 whole-slide metastases and primary colorectal tumors from 222 patients. Primary lesions, and synchronous and metachronous metastases, had a heterogeneous immune infiltrate and mutational diversity. Small metastases had frequently a low Immunoscore and T and B cell score, while a high Immunoscore was associated with a lower number of metastases. Anti-epidermal growth factor receptor treatment modified immune gene expression and significantly increased T cell densities in the metastasis core. The predictive accuracy of the Immunoscore from a single biopsy was superior to the one of programmed cell death ligand 1 (PD-L1). The immune phenotype of the least-infiltrated metastasis had a stronger association with patient outcome than other metastases.

INTRODUCTION

Over 90% of colorectal cancer (CRC) patients with synchronous metastases die within 5 years of diagnosis (Jemal et al., 2008) and therefore a better understanding of metastatic development is needed. The extensive interactions between tumor cells and surrounding tissues during their dissemination complicate efforts to dissect the metastatic process. Metastatic cells must successfully negotiate complex steps leading to their establishment in a foreign tissue microenvironment. The acquisition of genomic alterations or behavioral changes does not completely explain this process, which is likely to be influenced not only by the tumor cells, but also the tumor microenvironment (Prendergast and Jaffee, 2007). Metastatic traits could be acquired by

Significance

This comprehensive analysis of patients with a complete resection of all metastases reveals the heterogeneity of the colorectal metastatic disease and its clinical impact. Complex tumor immune interrelations shape the metastatic landscape, not only in terms of number and size of lesions, or mutational pattern, but also in terms of immune cell infiltrate. Adaptive immune cells and Immunoscore quantified in the least-infiltrated metastasis per patient are the most associated with patient long-term survival. This intra-metastatic adaptive immune reaction increases following a neoadjuvant treatment, an effect that could be therapeutically exploited to improve the survival of metastatic patients.

exposure of cancer cells to paracrine signals received from the microenvironment (Langley and Fidler, 2007; Prendergast and Jaffee, 2007). Due to the complexity and heterogeneity of tumors (Alizadeh et al., 2015; Bindea et al., 2010; Galon et al., 2006, 2013; Pages et al., 2005; Wang et al., 2004), the role of the tumor microenvironment within metastases has been difficult to determine. We previously reported the major role of cytotoxic and memory T lymphocytes within primary tumors in predicting survival of cancer patients (Galon et al., 2006; Mlecnik et al., 2011; Pages et al., 2018), including early-stage cancer patients (Pages et al., 2009), and we defined mechanisms resulting in changes of specific immune cell densities within the tumor (Mlecnik et al., 2014). A scoring system designated "Immunoscore" based on the quantification of two lymphocyte populations in the core (CT) and at the invasive margin (IM) of primary tumors has a prognostic value superior to the AJCC/UICC TNM-classification (Galon et al., 2006, 2012, 2014; Pages et al., 2018). Immunoscore and lymphatic vessels from primary tumors are protective against the generation of distant metastases (Mlecnik et al., 2016b), and we have shown that Immunoscore predicts survival of metastatic patients (Berghoff et al., 2016; Mlecnik et al., 2018). Furthermore, we have demonstrated the superiority of Immunoscore over microsatellite instability in predicting survival (Mlecnik et al., 2016a).

Currently, liver CRC metastases resection dramatically improves long-term survival and offers potential for a cure. Nevertheless, 70% of patients with curatively resected metastasis relapse and half of these recurrences will be fatal (Jemal et al., 2008). The treatment decision is often based on a single biopsy that may not reflect the overall portrait of the patient's disease. The immune microenvironment and Immunoscore of synchronous and metachronous metastases from CRC patients have not yet been fully investigated.

RESULTS

Metastases and Primary Tumors Have a Heterogeneous Immune Environment and Somatic Mutation Profile

Global (whole-slide) and 3 hotspot (3HS) densities from lymphocyte subsets were analyzed in the CT and IM of 603 metastases and 97 available primary tumors from 222 CRC patients (cohorts 1 and 2). Among the 338 metastases analyzed in cohort 1, a total of 37.7 million CD3 T cells were counted by digital pathology. The mean number of CD3 T cells counted on a metastasis was 115,000 T cells per tumor slide. Given the mean sizes of all the 338 metastases, one can extrapolate that, on average, a metastasis contains 322 million CD3 T cells. Figure 1A illustrates MRI and fluoro-2-deoxyglucose positron emission tomography images of synchronous and metachronous metastases of a patient. Intra-metastatic CD3 cells and the corresponding density heatmap plot in the CT and IM are shown for a metastasis. CD3 densities varied in each tile area of the metastasis, suggesting intra-metastatic immune heterogeneity, as shown in Figures 1B and S1A. The most-infiltrated metastasis of this patient had 13,746 CD3-positive cells/mm^2 in the CT, while the least-infiltrated metastasis had only 1,134 CD3 cells/mm^2 (Figure S1A). Moreover, the heterogeneity of CD3, CD8, CD45RO, FOXP3 T lymphocytes, and B cell densities was observed in the CT and IM between metastases from the same patient (Figures 1C and S1A), as well as between patients (Figures 1D, S1B, and S1C). As previously demonstrated in primary tumors, adaptive immune subpopulations correlated within a metastatic region as illustrated for the CT (Figures S1D and S1E), as well as between metastatic regions (Figures S1F and S1G).

To further define inter-metastatic differences, a cancer hotspot mutation panel (n = 288) was tested in 12 patients (8 primary tumors, 56 metastases from cohort 1) with a diverse immune infiltrate. In addition, the Immunoscore was calculated for each of these metastases based on CD3 and CD8 densities in 3HS of the CT and IM. Mutations were found in 13 out of 50 cancer genes including *PIK3CA*, *APC*, *TP53*, and *KRAS* (Table S1; Figure S2), and differed between primary tumors and metastases (e.g., patients P210, P211). The unsupervised clustering of mutational data revealed two main groups of metastatic lesions and primary tumors (Figures 2A) that had a different immune infiltrate and Immunoscore (Figure 2B, $p < 0.05$). Cluster 2 was mainly associated with a germline variant of *KDR* (Q472H) and *PIK3CA* mutation (I391M), and had a higher CD8 infiltrate and Immunoscore. The Q472H alteration variant appeared to increase vascular endothelial growth factor receptor 2 (KDR) phosphorylation and hence to higher levels of vascular endothelial growth factor (VEGF) secretion and microvessel formation (Silva et al., 2016), which could promote lymphocyte chemotaxis and localization of T cells at the tumor site (Edelbauer et al., 2010). This could explain the higher association of Immunoscore with the germline variant of KDR (Q472H) observed in our cohort. Interestingly, similar to the immune heterogeneity, an inter-metastatic heterogeneity of mutations was observed (Figure 2C).

The Immunoscore was generally heterogeneous between metastases from the same patient (Figures 3A and S3A–S3C). Intratumoral heterogeneity of the metastases was also investigated in relation with patient prognosis using randomly selected metastases. The CD3, CD8, and CD20 hazard ratio (HR) values at median cutoff for disease-free survival (DFS) and overall survival (OS) were calculated for each percentile step, were all above 1.45, and significantly associated with clinical outcome (Figure S3B). Comparison of all HRs revealed that the best prediction of OS was observed around the median percentiles of CD8 (maximum at 55%), indicating that CD8 should be homogeneously distributed within a metastasis and at high density to be better associated with prolonged survival (Figure S3B). In contrast, CD20 B cell analysis showed that the best prediction of OS was observed at low percentiles (5%–35%) indicating that regions with few CD20 B cells are more associated with prolonged OS than those with absence of B cells (Figure S3B). Finally, the association between spatial heterogeneity and survival was investigated using patient groups stratified at the median of the standard deviation of the density for each marker (Figure S3C). The results confirmed that a high spatial heterogeneity of CD8 was associated with a significantly worse outcome (DFS, OS) (Figure S3C).

Consequentially, immune cell densities were investigated in relation to metastasis size, metastatic burden, and location. Interestingly, the 3HS and global immune densities presented different patterns depending on the size of the metastases. While global average immune densities were significantly higher in smaller metastases, the 3HS immune densities, representing areas of maximum infiltration, were higher in the larger metastases, with the exception of CD20 and FOXP3 in the IM

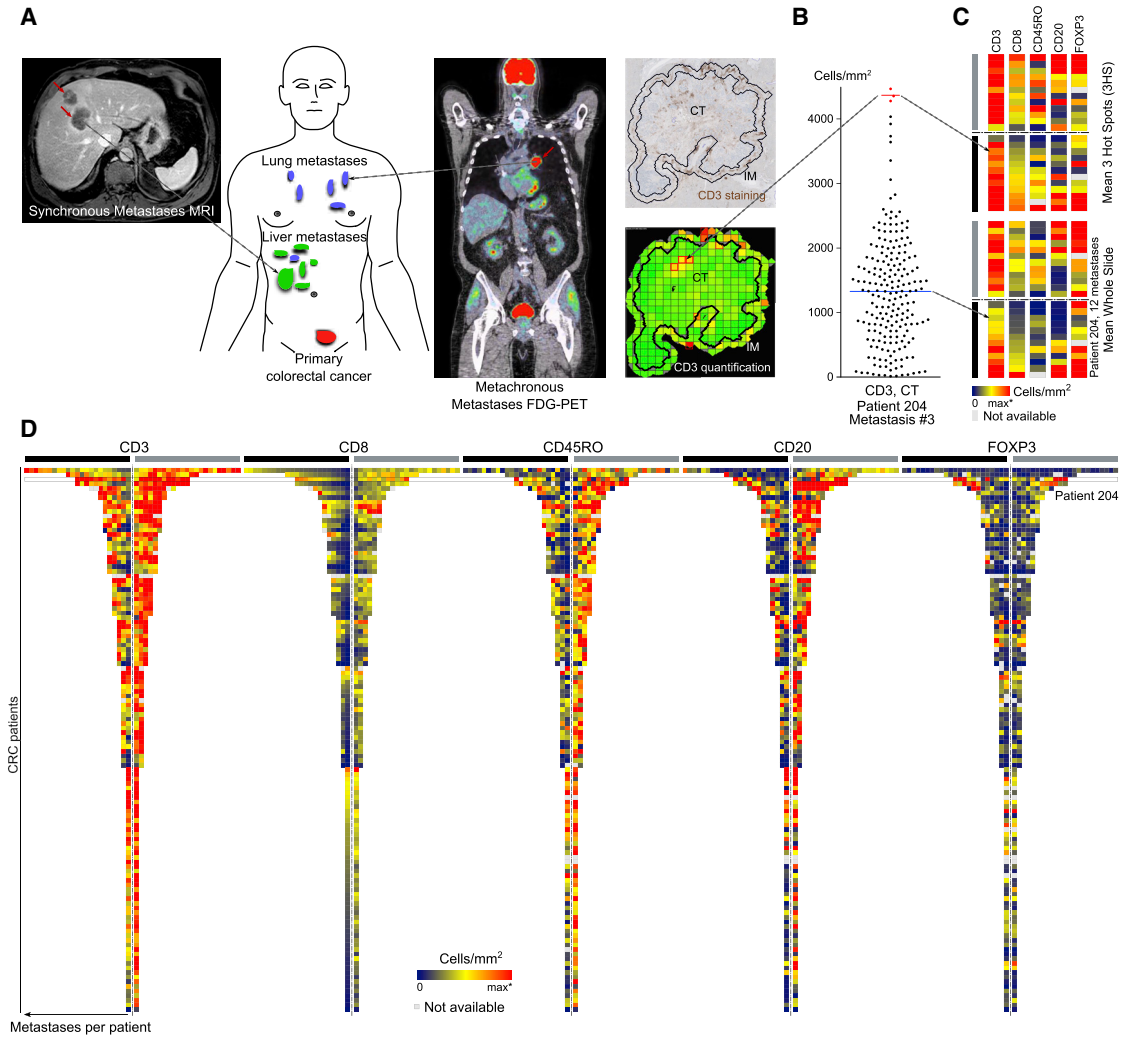

Figure 1. Immune Infiltrate of the Metastasis, and the Inter- and Intra-metastatic Heterogeneity

(A) MRI and 2-[(18)F] fluoro-2-deoxyglucose positron emission tomography (FDG-PET) in the diagnosis of synchronous (green) and metachronous (blue) liver and lung metastases in a CRC patient. A representative whole-slide immunohistochemical staining of the immune infiltrate (CD3 in brown, top) and an automatic CD3 quantification in tiles from each region (bottom) in a metastasis from patient 204 are shown. The center (CT) and the invasive margin (IM) of the metastasis were defined. Low and high CD3 densities are shown with a color gradient scaling from green to red. The three most-infiltrated tiles (3 hotspots [3HS]) from each region are marked in red.

(B) Each dot represents the CD3 density in one analyzed tile from the CT of the analyzed metastasis in (A). 3HS are shown as red dots. Mean values of all and the 3HS are indicated with a blue and a red dash, respectively.

(C) The heatmap shows the mean density over the 3HS (top) and whole slide (bottom) in the CT (black) and IM (gray) of each of the 12 metastases of patient 204. Metastases were sorted based on the CD8 CT density. The same order was applied to all the other markers. The heatmap was mirrored at the dashed line.

(D) The intra-metastatic immune cell densities were calculated from the 3HS in the CT and IM of each metastasis for each patient from cohort 1 (n = 114 patients). Patients were sorted based on the number of metastases. Groups of patients with the same number of metastases were sorted based on the CD8 CT density of the lowest-infiltrated metastasis. The CD8 CT metastasis order was also applied to the IM and all the other markers. The heatmap was mirrored at the dashed line (CT in black, IM in gray). Immune densities were visualized in Genesis and are ranging from low (blue) to high (red). Maximum densities were 5,000 cells/mm^2 for CD3, CD8, and CD45RO, 1,600 cells/mm^2 for CD20, and 500 cells/mm^2 for FOXP3. Missing values are shown in light gray.

See also Figure S1.

(Figures 3B, 3C, and S3A). Similar results were found when analyzing the smallest or largest metastasis for patients with multiple metastases. A high Immunoscore (I3–4) was significantly associated with large metastases and a low Immunoscore (I0–2) was more frequent in small metastases (Figure 3D). Tumor size was not influencing the DFS (Figure S3D). High Immunoscore patients had a significantly prolonged survival even if they had large tumors (Figure S3D). Analysis of the least-infiltrated metastasis revealed that patients with only one metastasis had a significantly higher immune infiltration in both the CT and IM (Figures 3F and 3G). However, analysis of the highest immune infiltrated metastasis showed that patients with a large number of metastases had significantly higher average immune cell densities in these metastases than patients with only a few metastases

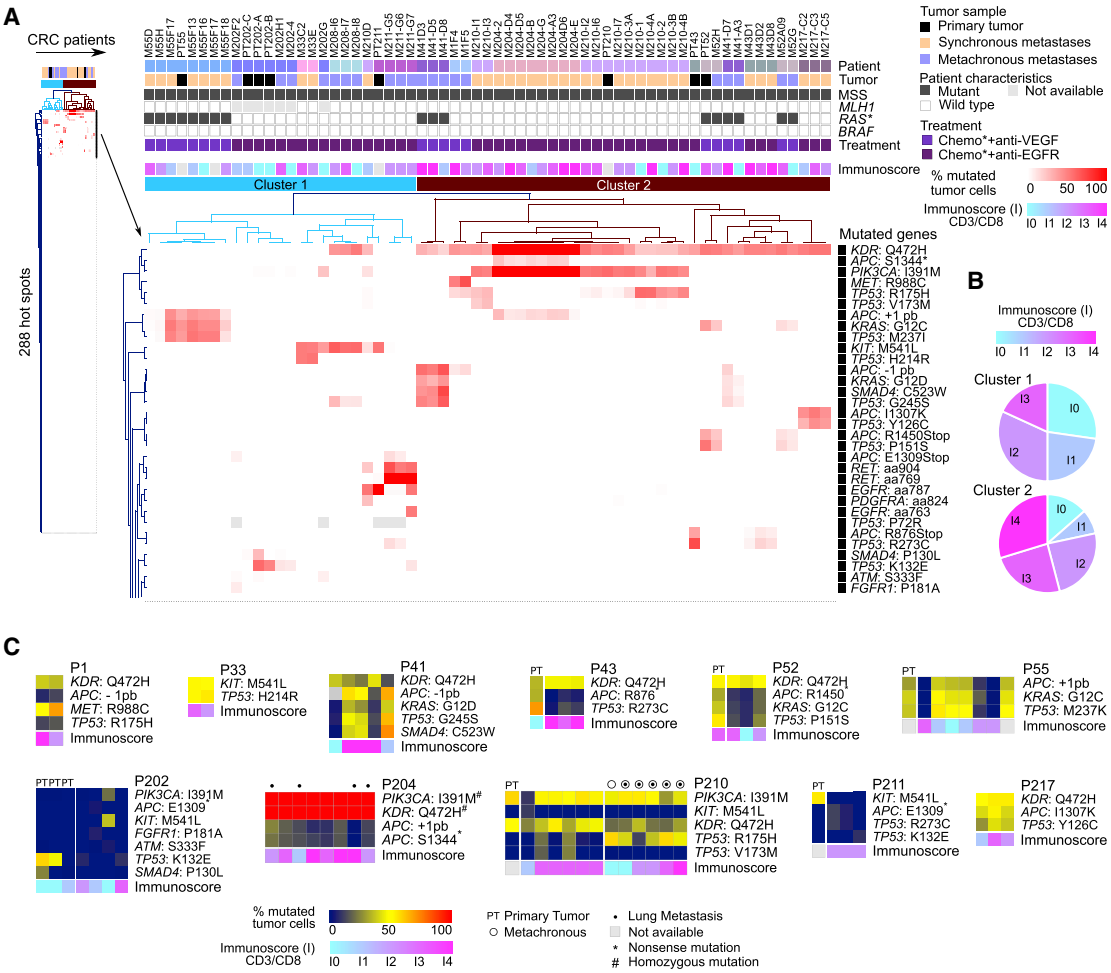

Figure 2. Mutations of Known Cancer Genes in Metastases from CRC Patients

(A) Unsupervised hierarchical clustering (Pearson distance, complete linkage) of mutations of 50 cancer-related genes in metastases and primary tumors from 12 CRC patients from cohort 1 are shown. Primary tumors, and synchronous and metachronous metastases are marked in black, beige, and light blue, respectively. The percentage of mutated tumor cells is shown with a red gradient. Absence of mutation is shown in white. Patient characteristics such as the microsatellite status, *RAS* (Allegra et al., 2016), and *BRAF* mutational status and treatment, are shown together with the tumor sample type and the Immunoscore, which was calculated in each metastasis. Microsatellite stable (MSS) patients, *RAS* and *BRAF* mutations are shown in black. Patients treated with chemotherapy (oxaliplatin or irinotecan and fluoropyrimidines) and anti-VEGF or anti-EGFR are shown with light and dark purple, respectively. Immunoscore was calculated based on 3HS CD3, and CD8 densities from the CT and IM of metastases. Immunoscore categories I0, I1, I2, I3, and I4 are shown with a color gradient scaling from azure (I0, low) to pink (I4, high). Two sample clusters are marked in azure and dark red, respectively.

(B) The frequency of Immunoscore groups in clusters 1 and 2.

(C) Representative examples of the mutational profiles. Primary tumor (PT), lung metastasis (●), and metachronous metastasis (□) are marked, no indication corresponding to synchronous liver metastasis. The percentage of mutated tumor cells for *APC*, *KIT*, *KDR*, *KRAS*, *MET*, *PIK3CA*, and *TP53* is shown with a gradient scaling from blue (0%) to red (100%). The nonsense and homozygous mutations are marked with * and #, respectively.

See also Figure S2 and Table S1.

($p < 0.05$). Nevertheless, there was no difference in the mean immune infiltrate of patients with different metastatic burden. A high Immunoscore, measured using 3HS of the least-infiltrated metastasis was associated with a significantly lower number of metastases (Figure 3H) and prolonged survival (Figure 3I), while patients with increased metastatic burden had a lower Immunoscore ($p < 0.001$) (Figure 3H). Subsequent comparison of lung versus liver metastases showed no difference in Immunoscore within metastases between these two sites (Figure S3E).

Higher densities of CD3, CD8, CD45R0, and CD20 were observed at the IM compared with CT in a subgroup of patients with paired synchronous (Figures 4A and S4A) or metachronous (Figures 4B and S4B) resection of metastases and their primary tumors or in the entire cohort 1 (Figure 4C). Similarly, significantly higher densities of CD3, CD8, and CD45R0 were quantified in metastases compared with primary tumors (Figures 4C and 5A). Significantly lower CD20 densities infiltrated the CT of metastases compared with primary tumors. A similar trend was observed for FOXP3. Metastases and primary tumors have thus a heterogeneous immune environment and mutational profile. Comparison of synchronous with metachronous metastases was not different (Figure 4C).

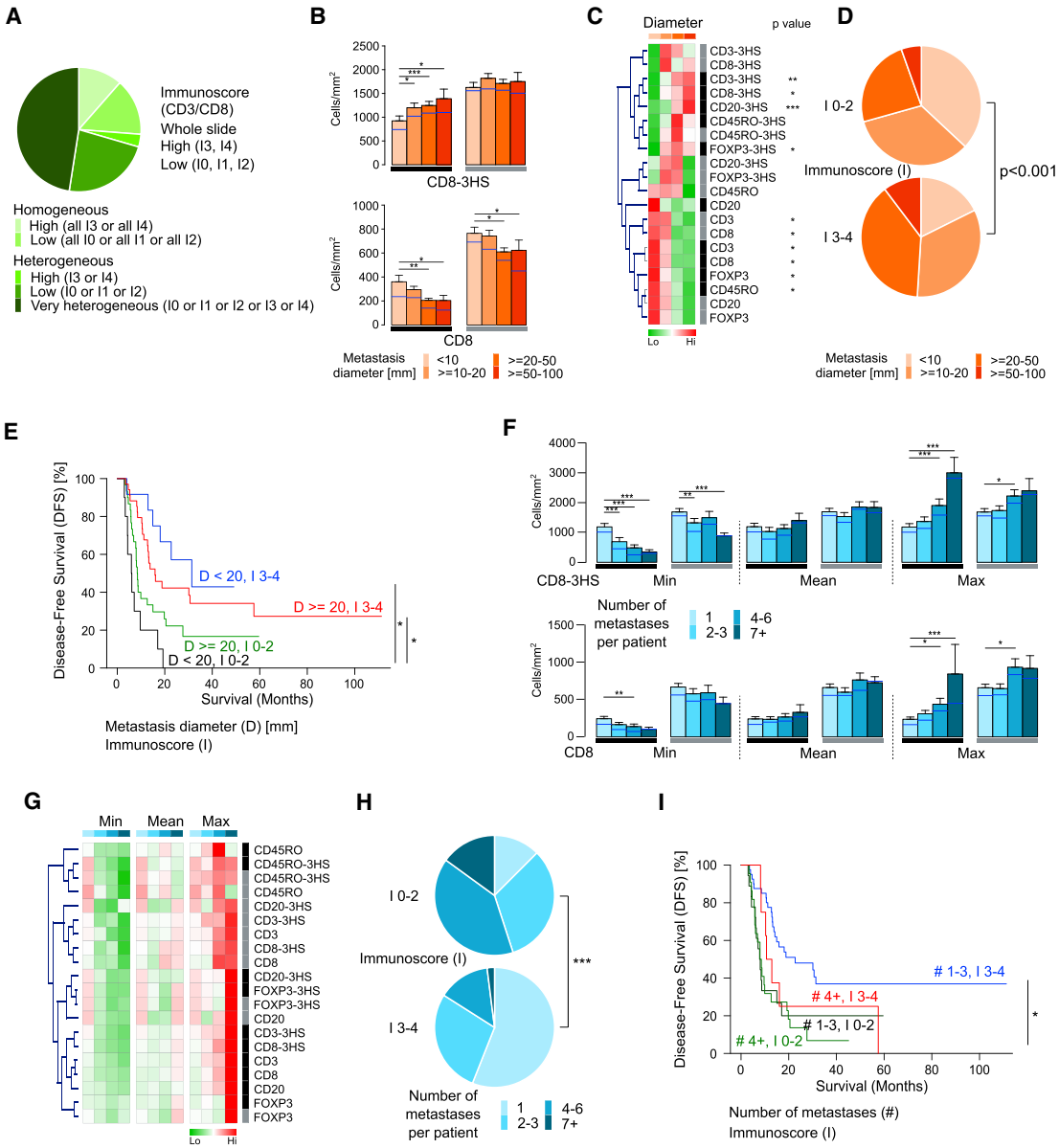

Figure 3. Metastasis Heterogeneity, Burden, Size, and the Immunoscore

(A) The Immunoscore (CD3/CD8) was measured from the whole slide in all metastases from each of the patients who had at least two metastases. Metastasis infiltration was considered homogeneous only if all metastases of the patient had the same Immunoscore. Homogeneous high: all metastases were I3 or I4; homogeneous low: all metastases were I0, I1, or I2; heterogeneous high: metastases were I3 and I4; heterogeneous low: metastases were I0, I1, and I2; very heterogeneous: metastases had all Immunoscores. The percentage of patients with different degree of Immunoscore heterogeneity was represented with a gradient scaling from light (high homogeneous) to dark (very heterogeneous) green.

(B) 3HS (top) and whole-slide (bottom) CD8 densities from the CT (black) and IM (gray) in patient groups defined based on metastasis diameter. Groups are shown with a color gradient scaling from light (<10 mm) to dark (≥50–100 mm) orange. Bar charts represent the mean ± SEM and the median cell count/mm^2 is shown as a blue line. Wilcoxon-Mann-Whitney test was applied.

(C) Mean 3HS and whole-slide immune densities from CT (black) and IM (gray) *Z* score normalized and hierarchically clustered (Euclidean distance, complete linkage). Patient groups are defined based on metastasis diameter. Low (green), high (red).

(D) The percentage of metastases with different size in Immunoscore groups. Fisher's exact test was applied.

(E) Kaplan-Meier estimates of disease-free survival (DFS) according to the metastasis diameter in combination with the Immunoscore.

(F) 3HS (top) or whole-slide (bottom) CD8 densities from the CT (black) and IM (gray) measured in patient groups defined based on the number of metastases. Groups are shown with a color gradient ranging from light (1 metastasis) to dark (>7 metastases) azure. Mean, mean density per patient; Min, the lowest infiltrated metastasis per patient; Max, the highest infiltrated metastasis of each patient. Bar charts represent the mean ± SEM and the median is shown as a blue line. Wilcoxon-Mann-Whitney test was applied.

(legend continued on next page)

Neoadjuvant Treatment Impacts Gene Expression, Intratumoral Immune Cell Density, and Immunoscore

Samples from 48 patients (cohorts 1 and 2) with synchronous resection of metastases and primary tumors receiving no preoperative treatment or treatment with chemotherapy alone or chemotherapy in combination with anti-epidermal growth factor receptor (EGFR) or anti-VEGF were also investigated. Independent of the treatment, CD3, CD8, and CD45RO densities were significantly increased in the IM of the metastases (Figure 5A), but not in the primary tumors. Compared with untreated patients, the administration of chemotherapy in combination with anti-EGFR increased the CD8 infiltrate level not only in the IM but also in the CT of metastases (Figures 5B and 5C). Surprisingly, this effect was not observed for metastases from patients treated with chemotherapy and anti-VEGF (Figure 5C). Instead, chemotherapy + anti-VEGF appeared to be associated with higher B cell densities in the primary tumors (Figures 5A and 5C). In contrast, metastases treated with chemotherapy and anti-EGFR showed significantly higher densities of immune cells compared with no treatment, chemotherapy alone, or chemotherapy and anti-VEGF ($p < 0.05$) (Figure 5D), reflecting a global boost of cytotoxic (CD8), effector memory (CD45RO), and regulatory (FOXP3) T (CD3) cells in the tumor microenvironment of these patients. In contrast to other treatments, higher regulatory T cell (FOXP3) densities were only observed following anti-EGFR treatment in the primary tumors (Figure 5C). In addition, a significantly higher density of programmed cell death 1 (PD1) cells infiltrated the CT and IM of treated metastases (Figure S5A). This effect was not observed in primary tumors, or for programmed cell death ligand **1** (PDL1) (Figure S5B) or macrophages (CD68) (Figure S5C) in both metastatic regions.

RAS mutated patients had significantly less intra-metastatic immune infiltrates than wild-type (WT) lesions (Figure S5D). In this retrospective cohort, these patients were included in all treatment categories (Figure S5E). *RAS* mutational status was not influencing the immune infiltrate of untreated patients (Figure S5F) or their survival (Figure S5G). In contrast, *RAS* WT samples were significantly more infiltrated with CD3, CD8, and CD45RO cells following chemotherapy + anti-EGFR (Figure S5H).

Strikingly, the strongest increase of immune densities in the treated patient samples was observed in the highest infiltrated metastasis (Max), while the mean infiltration of metastases showed only a slight increase after anti-EGFR treatment, and the least-infiltrated metastasis (Min) showed no significant changes (Figures 5E and 5F). These results suggest that the treatment could be more efficient in increasing the intra-metastatic immune reaction in metastases with pre-existing immune infiltrate. Indeed, a high Immunoscore (I3–4), measured as the mean metastatic immune infiltrate, had a significantly higher frequency in chemotherapy and anti-EGFR-treated patients compared with other preoperative treatments (Figure 5G).

The impact of treatment with anti-VEGF or anti-EGFR on the tumor microenvironment was further investigated in biopsies from rectal cancer tumors (cohort 3, n = 16; cohort 4, n = 40) (Debucquoy et al., 2009; Verstraete et al., 2015). CluePedia (Bindea et al., 2013a) and ClueGO (Bindea et al., 2009) were used to compare gene expression levels before and after one dose of anti-EGFR or anti-VEGF (Figures 6A and 6B). As expected, anti-VEGF treatment resulted in decreased expression of *CXCL8*, a mediator of the inflammatory response, angiogenesis, collagen-related genes, and adhesion molecules (Figure 6A). A similar trend was observed for genes involved in chemotaxis (*CXCL9*, *CXCL10*, and *CXCL11*). Moreover, anti-VEGF treatment increased expression levels of B cell and natural killer cell genes, as well as genes related to innate cell chemotaxis or complement. On the other hand, anti-EGFR treatment increased granzyme B (*GZMB*) expression, suggesting an induction of antibody-dependent cellular cytotoxicity or enhanced CD8 T lymphocyte function (Figure 6B). Immune activation by anti-EGFR was further implicated by increased expression of complement components, suggesting an increased recruitment and activation of effector cells. These observations are in accordance with the increased immune densities observed after anti-EGFR treatment in cohorts 1 and 2 (Figures 5C and 5D).

Both treatments influenced inflammatory responses and increased the expression of complement components, but their impact on the tumor microenvironment was likely different since they targeted different pathways (Figure S6A). In addition to the anti-tumor impact, the anti-EGFR treatment increased expression of immune components in the microenvironment, as illustrated with the Immunome (Bindea et al., 2013b) (Figure S6B). Out of all genes associated with the type I interferon signaling pathway, only *EGR1* was significantly downregulated after the treatment (Figure S6C).

Immune Infiltrate and Immunoscore are Associated with Patient Outcome

Immune densities, Immunoscore and T and B cell score (TB score) (CD8 and CD20) from the least- and most-infiltrated metastasis, a randomly chosen metastasis as well as the mean across all metastases, were further investigated in relation to patient outcome in cohorts 1 (training) and 2 (validation) (Figures 7A–7C and S7A–S7C). No significant differences were observed between the two cohorts except for preoperative treatments. In both cohorts (using the same density cutoff of cohort 1 for the validation of cohort 2), high immune infiltrate, Immunoscore and TB score were significantly associated with prolonged patient survival (Figures S7A–S7C) and decreased relapse incidence (Figures 7A–7C). The least-infiltrated metastasis showed the strongest association with patient outcome compared with the mean metastatic infiltrate or a randomly selected metastasis from cohorts 1 and 2 (Figures 7C and S7C). In both cohorts, the infiltrates of the randomly selected metastases or the mean of all metastases were significant but less accurately predicting the

(G) Mean 3HS and whole-slide immune densities from CT (black) and IM (gray) *Z* score normalized and hierarchically clustered (Euclidean distance, complete linkage). Patient groups are defined based on the number of metastases. Low (green), high (red).
(H) The percentage of patients having one or more metastases in Immunoscore groups.
(I) Kaplan-Meier estimates of DFS according to the number of metastases in combination with the Immunoscore.
***$p < 0.005$, **$0.005 \leq p < 0.01$, *$0.01 \leq p < 0.05$. See also Figure S3.

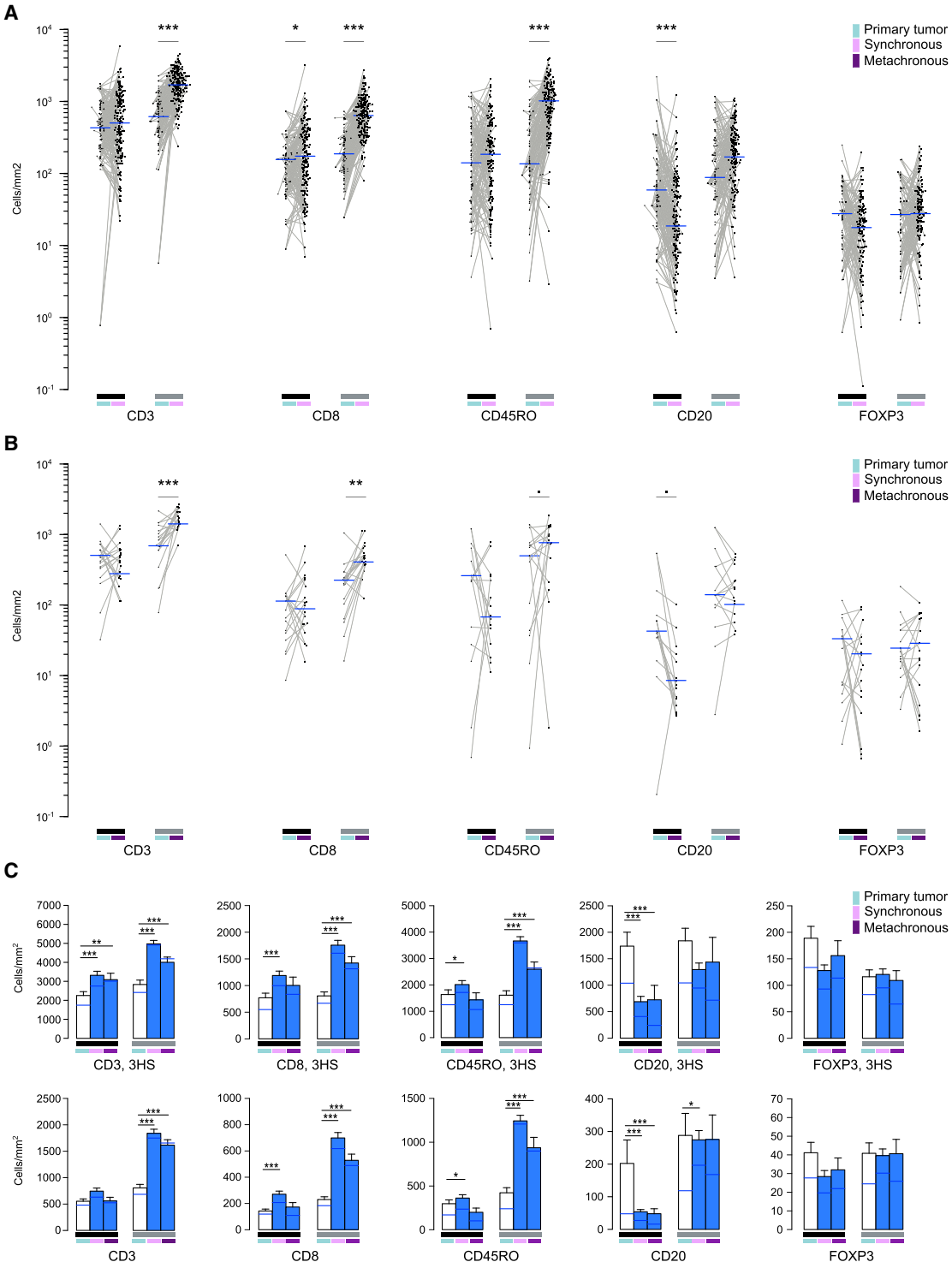

Figure 4. Immune Densities in Primary Tumors versus Synchronous and Metachronous Metastases

(A and B) Whole-slide densities are shown in a paired fashion between primary tumors (azure) and corresponding synchronous (A, pink) or metachronous (B, purple) metastases. The median is shown as a blue line. The significance test is based on a multilevel linear mixed-effects model (lme). ***$p < 0.005$, **$0.005 \leq p < 0.01$, *$0.01 \leq p < 0.05$, ■ $0.05 \leq p < 0.1$.

(C) 3HS (top) or the whole-slide (bottom) immune cell densities from CT (black) and IM (gray) of metastases (purple) and primary tumors (azure) of the entire cohort 1 (114 patients, 338 metastases, 69 primary tumors). Bar plots represent the mean ± SEM densities over all metastases of a patient, and the median as a blue line. Wilcoxon-Mann-Whitney test was applied.

See also Figure S4.

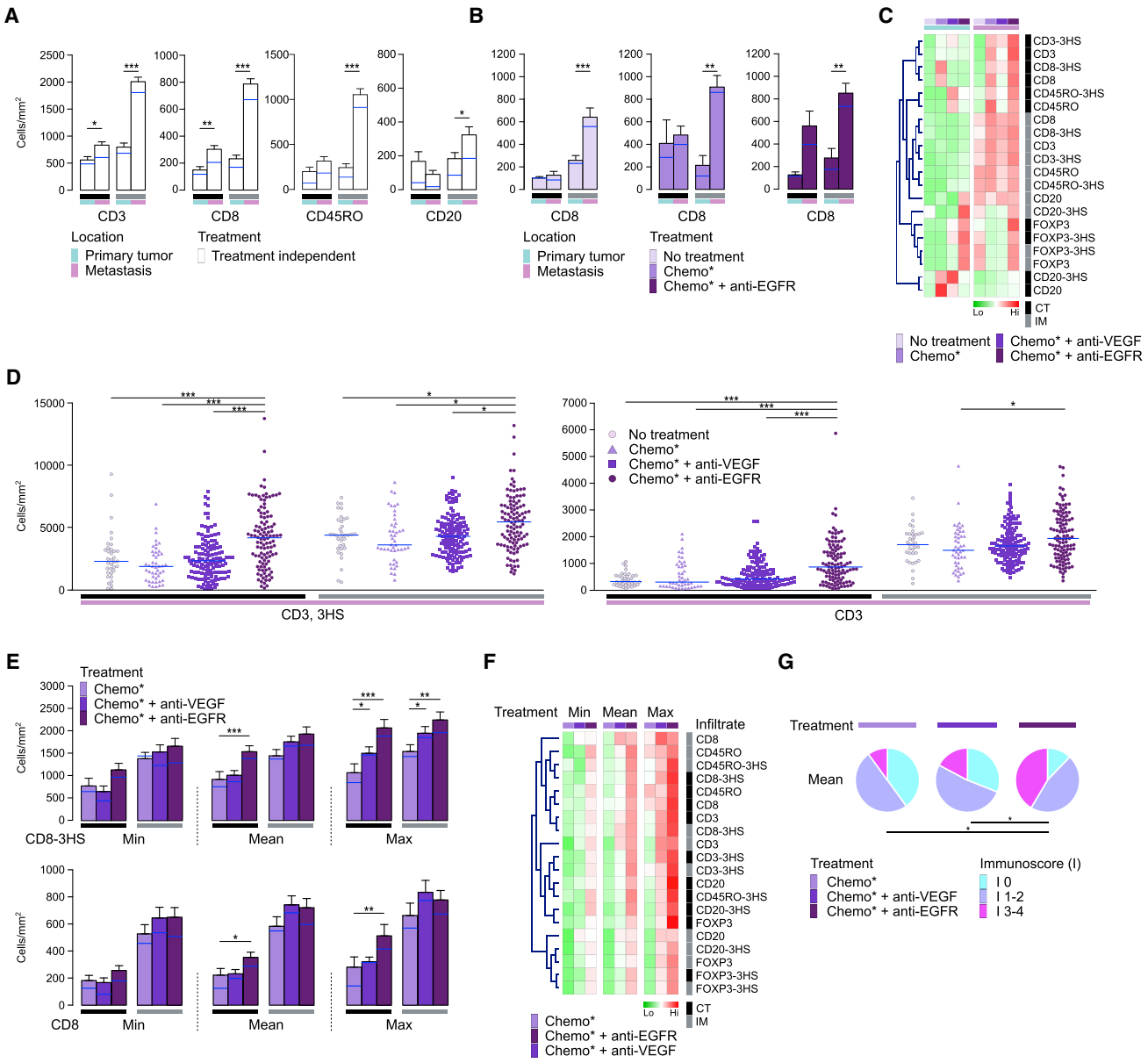

Figure 5. Immune Cell Densities, Immunoscore, and the Response to Treatment

(A) Whole-slide immune densities from CT (black) and IM (gray) of metastases (purple) and primary tumors (azure) from treatment-independent patients (149 metastatic lesions from 48 patients). Bar plots represent the mean ± SEM densities over all metastases of a patient, and the median as a blue line. The significance test is based on a multilevel linear mixed-effects model (lme).

(B) Whole-slide intra-metastatic CD8 densities ± SEM from not treated patients (left; 16 patients, 20 metastases) or from patients receiving the same treatment before primary tumor and metastasis resection: neoadjuvant chemotherapy (oxaliplatin or irinotecan and fluoropyrimidines) alone (middle; 9 patients, 20 metastases) or in combination with anti-EGFR (right; 10 patients, 28 metastases). The significance test is based on a multilevel linear mixed-effects model (lme).

(C) Mean 3HS and whole-slide immune densities from CT (black) and IM (gray) of primary tumors (azure) and metastases (purple), *Z* score normalized and hierarchically clustered (Euclidean distance, complete linkage). Patient groups based on the treatment: no treatment; chemotherapy alone; chemotherapy and anti-VEGF (13 patients, 81 metastases); and chemotherapy and anti-EGFR are shown with a color gradient scaling from light to dark purple. Low (green), high (red).

(D) Dot plot for 3HS and whole-slide intra-metastatic CD8 densities in treatment-based patient groups (entire cohort 1). The mean values are indicated by blue dashes. The significance test is based on a multilevel linear mixed-effects model (lme).

(E) Bar plots represent the mean 3HS (top) and whole-slide (bottom) densities ± SEM from metastases of treated patients (entire cohort 1), and the median as a blue line. Mean, mean density per patient; Min, the lowest infiltrated metastasis per patient; Max, the highest infiltrated metastasis of each patient. The Wilcoxon-Mann-Whitney test was applied.

(legend continued on next page)

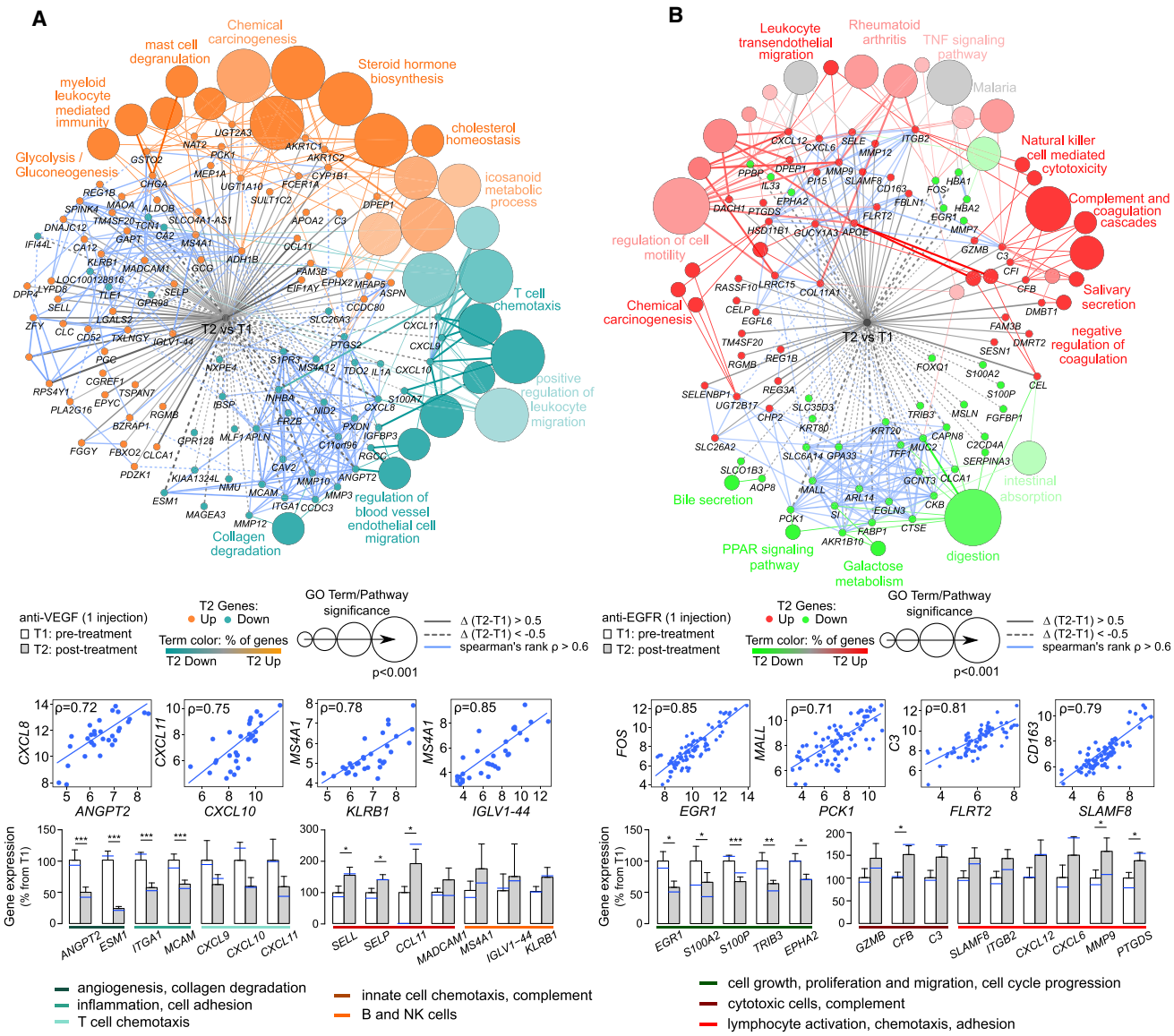

Figure 6. Biological Role of Genes Modified after Anti-EGFR or Anti-VEGF Treatment

(A and B) ClueGO/CluePedia networks of modified genes after one injection with anti-VEGF (cohort 3, A) or anti-EGFR (cohort 4, B), and their biological role. Genes with a Δ expression difference after the treatment >0.5 are shown. Δ is shown as gray edges, negative Δ are discontinuous lines. Spearman rank correlation values > 0.6 are shown as blue edges. The pathway color gradient shows the proportion of associated genes with increasing (A, orange; B, red) or decreasing (A, dark green; B, green) expression. Equal proportion is shown in gray. The size of the pathway nodes shows the term significance (right-sided hypergeometric test, Bonferroni step-down correction). Fusion was applied to reduce the redundancy. The Organic algorithm was used for organizing the networks. Examples of CluePedia correlation plots are shown. Bar charts represent the mean expression level (relative to the not treated sample) ± SEM. A parametric or nonparametric test was applied based on the Shapiro normality test. ***p < 0.005, **0.005 ≤ p < 0.01, *0.01 ≤ p < 0.05. See also Figure S6.

DFS and OS (Figures 7C and S7C), and no association with the patient survival was observed for the most-infiltrated metastasis. The metastasis with lowest immune infiltration therefore represented the most important prognostic factor for patient tumor relapse, OS and DFS (HR > 2, p < 0.05).

Biopsy Simulations Accurately Estimate the Intra-metastatic Immune Infiltrate

The accuracy of biopsies in estimating the metastatic immune infiltrate (Figure 8A) and the survival of the patient was next investigated. A tile (CT or IM) has a surface of ~0.64 mm^2

(F) Mean 3HS and whole-slide immune densities from CT (black) and IM (gray) *Z* score normalized and hierarchically clustered. Patient groups based on the treatment. Low (green), high (red).

(G) The percentage of Immunoscore categories in treatment based groups. Fischer's exact test was applied.

***p < 0.005, **0.005 ≤ p < 0.01, *0.01 ≤ p < 0.05. See also Figure S5.

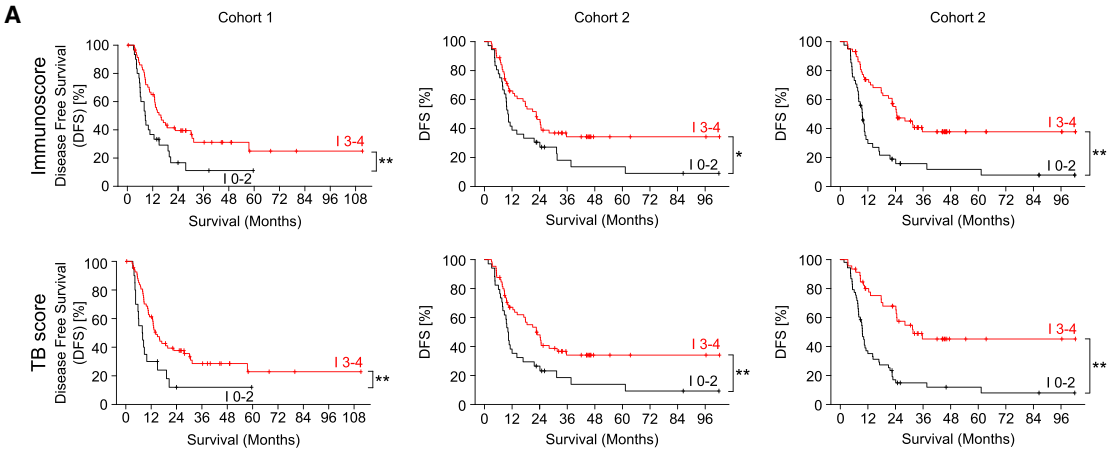

B

Immune densities, whole slide, Min metastasis	DFS Events/Total Cohort 1	Hazard Ratio (95% CI)	Wald p value	DFS Events/Total Cohort 2	Hazard Ratio (95% CI)	Wald p value
CD3 CT Hi vs Lo	63/89	1.93 (1.13–3.29)	0.0160	68/99	1.68 (1.0–2.82)	0.0480
CD3 IM Hi vs Lo	63/89	1.57 (0.91–2.72)	0.1040	68/99	1.29 (0.8–2.09)	0.3022
CD8 CT Hi vs Lo	64/90	2.01 (1.14–3.52)	0.0150	68/99	1.86 (1.14–3.02)	0.0125
CD8 IM Hi vs Lo	64/90	1.94 (1.06–3.56)	0.0315	68/99	1.37 (0.76–2.48)	0.2976
CD20 CT Hi vs Lo	63/89	1.89 (1.13–3.15)	0.0147	68/99	1.87 (1.16–3.01)	0.0105
CD20 IM Hi vs Lo	63/89	1.63 (0.87–3.06)	0.1297	68/99	1.78 (1.02–3.09)	0.0411
Immunoscore I 3-4 vs I 0-2	63/89	1.94 (1.16–3.22)	0.0111	68/99	1.77 (1.1–2.87)	0.0198
Immunoscore I 4 vs I 2-3	63/89	1.7 (0.92–3.12)	0.0882	68/99	1.39 (0.78–2.49)	0.2633
I 4 vs I 0-1		2.6 (1.25–5.41)	0.0106		1.99 (1.1–3.6)	0.0234
TB score TB 3-4 vs TB 0-2	63/89	2.08 (1.18–3.64)	0.0109	68/99	1.92 (1.18–3.11)	0.0085
TB score TB 4 vs TB 2-3	63/89	1.72 (1.0–2.97)	0.0495	68/99	2.19 (1.27–3.78)	0.0048
TB 4 vs TB 0-1		2.62 (1.26–5.44)	0.0100		2.44 (1.25–4.77)	0.0091

C

Immune densities 3 Hot Spots	DFS Events/Total Cohort 1	Hazard Ratio (95% CI)	Wald p value	DFS Events/Total Cohort 2	Hazard Ratio (95% CI)	Wald p value
CD8 CT-Min Hi vs Lo	64/90	2.75 (1.65–4.59)	0.0001	68/99	4.15 (1.66–10.36)	0.0023
CD8 CT-Rand Hi vs Lo	64/90	2.2 (1.25–3.86)	0.0064	68/99	2.94 (1.34–6.44)	0.0072
CD8 CT-Mean Hi vs Lo	64/90	2.27 (1.24–4.13)	0.0075	68/99	2.68 (1.37–5.25)	0.0042
CD8 CT-Max Hi vs Lo	64/90	0.65 (0.38–1.08)	0.0980	68/99	2.11 (1.3–3.44)	0.0026
CD8 IM-Min Hi vs Lo	64/90	2.61 (1.5–4.54)	0.0007	68/99	2.2 (1.01–4.82)	0.0482
CD8 IM-Rand Hi vs Lo	64/90	2.05 (1.08–3.86)	0.0272	68/99	1.69 (0.86–3.31)	0.1263
CD8 IM-Mean Hi vs Lo	64/90	1.67 (0.95–2.94)	0.0774	68/99	1.94 (1.14–3.31)	0.0141
CD8 IM-Max Hi vs Lo	64/90	1.45 (0.87–2.43)	0.1579	68/99	1.77 (1.08–2.91)	0.0239
Immunoscore-Min I 3–4 vs I 0-2	64/90	2.47 (1.49–4.07)	0.0004	68/99	9.22 (2.25–37.79)	0.0020
Immunoscore-Rand I 3–4 vs I 0-2	64/90	2.13 (1.27–3.6)	0.0044	68/99	3.75 (1.51–9.35)	0.0046
Immunoscore-Mean I 3–4 vs I 0-2	64/90	2.13 (1.15–3.94)	0.0157	68/99	2.3 (1.35–3.92)	0.0023
Immunoscore-Max I 3–4 vs I 0-2	62/88	1.67 (0.87–3.22)	0.1223	68/99	2.21 (1.37–3.58)	0.0012
TB score-Min TB 3–4 vs TB 0-2	63/89	3.21 (1.89–5.45)	<.0001	66/97	Inf(0–Inf)	NaN
TB score-Rand TB 3–4 vs TB 0-2	63/89	1.94 (1.18–3.21)	0.0094	68/99	4.76 (1.73–13.13)	0.0026
TB score-Mean TB 3–4 vs TB 0-2	63/89	2.26 (1.1–4.62)	0.0255	68/99	4.09 (1.87–8.97)	0.0004
TB score-Max TB 3–4 vs TB 0-2	63/89	1.1 (0.64–1.88)	0.7336	68/99	2.46 (1.49–4.07)	0.0005

Figure 7. The Risk to Relapse of Patients Based on the Least-Immune-Infiltrated Metastasis

(A) Kaplan-Meier curves for DFS of Immunoscore (I, CD3/CD8) and TB score are shown for the least-infiltrated metastasis per patient (left, cohort 1 with optimal cutoff; middle, cohort 2 with predefined optimal cutoff from cohort 1; and right, cohort 2 with optimal cutoff). Patients were grouped according to their

(legend continued on next page)

(0.8 × 0.8 mm), which comes close to a needle biopsy diameter of 20 gauge or three needle biopsies of 25 gauge. Real metastasis biopsies are often comprised between one and ten tiles depending on needle size and number of realized true-cuts. CD8 densities quantified in biopsies were compared with densities from metastasis tiles (Figure 8B). IM tiles are fewer but higher infiltrated than CT tiles, which reflected likely a biopsy punching the lesion core rather than its margin. The biopsy was representative for tumors with homogeneous infiltrate (e.g., P402), but it over- or underestimated the total immune infiltrate in heterogeneous tumors (P407, P30) and was less accurate in patients with inter-metastatic heterogeneity (P213).

From all metastatic CT tiles investigated (Figure 8A), a random tile was selected for each patient (cohorts 1 and 2) and the CD8 density was quantified. High or low patient groups were defined using the optimal cutoff of the marker at cohort level. The classification was compared with the reference based on the CD8 density from the minimum-infiltrated metastasis per patient. The study was then repeated 100 times. The simulation of a biopsy showed a very good specificity, low-infiltrated patients being correctly identified in more than 90% of the cases, even if a single tile was analyzed (Figures 8B–8G). To compare the one tile biopsy for sensitivity and specificity analysis of PDL1, CD3, CD8, and Immunoscore, only patients with complete datasets for all these markers were analyzed (Figure 8F). In more than 30% of these repetitions CD8 was log rank significant on the entire cohort level (Figure 8C). The sensitivity increased with the number of investigated tiles. At ten investigated tiles more than 80% of high-infiltrated patients were correctly classified, and the vast majority of these repetitions were log rank significant for DFS and OS (Figure S8). Similar results were obtained for CD3 and Immunoscore (Figures 8D and 8E). Sensitivity and specificity values obtained in cohort 1 were validated in cohort 2 (Figures 8C–8E). The evaluation of real biopsy taken before resection of the metastases confirmed the results obtained by the quantification of the whole metastatic slide (Figure 8B). In contrast, PDL1 evaluated from biopsies was less sensitive and specific (32%, 94% respectively) than CD3, CD8, or Immunoscore (65% and 99%, respectively) in estimating the reality of the positivity across the whole metastatic slide, as underlined by the concordance measured with the intraclass correlation, especially for low numbers of tiles (Figures 8F and 8G).

Biopsies thus represent only a static snapshot of a metastasis. A single metastatic biopsy identifies patients with a low immune infiltrate. Due to the heterogeneity of the metastatic disease, multiple biopsies may be needed to accurately estimate the intratumoral immune infiltrate, particularly for PDL1, and its impact on survival.

DISCUSSION

There is growing interest in personalized medicine and identifying prognostic and predictive biomarkers; however, the heterogeneity of an intratumoral host-immune response may foster tumor evolution and impede tailored treatment strategies.

T lymphocyte infiltrates and Immunoscore within colorectal primary tumors have significant prognostic value (Fridman et al., 2012; Galon et al., 2006, 2013; Pages et al., 2018) and protect against the generation of distant metastases (Mlecnik et al., 2016b). Here we report the immune and mutational characterization of all resected metastases from a cohort of patients with CRC. As in primary tumors (Bindea et al., 2013b), lymphocytes were found to infiltrate both the IM (Halama et al., 2011; Okano et al., 2003) and the metastatic CT. We characterized the multiverse of metastases and immune microenvironment and revealed the intra- and inter-tumor lesions and inter-patient heterogeneity of immune infiltrates for both primary tumors and metastases.

Mutational profiling showed heterogeneity between metastases and primary tumors, in concordance with the idea that tumors grow by clonal expansion and accumulating genetically diverse subpopulations (Gerlinger et al., 2012; Zhang et al., 2014). Beside genetic changes, the host immune response could influence the metastatic process (Angelova et al., 2018). Associations of mutations with increased immune infiltrate, cytolytic activity, and prolonged survival were previously described in primary tumors (Edelbauer et al., 2010; Manceau et al., 2015; Mlecnik et al., 2016a; Nosho et al., 2010; Rooney et al., 2015; Ziv et al., 2017). In such tumors, Immunoscore outperformed tumor molecular factors, such as microsatellite instability status in predicting survival (Mlecnik et al., 2016a). Interestingly, similar to the immune heterogeneity, an inter-metastatic heterogeneity of mutations was observed. Further studies are needed to elucidate how dynamics of genomic and immune patterns shape the CRC metastatic landscape.

Quantification of tumor-infiltrating lymphocytes in a small region of a randomly selected metastasis has previously been reported to be associated with survival (Halama et al., 2011; Katz et al., 2013; Kwak et al., 2016; Pugh et al., 2014; Tanis et al., 2015); however, the importance of analyzing the CT and IM regions of all resected metastases could be underlined by the fact that the tumor immune environment is heterogeneous. Several reports underlined the possible limitation of tumor sampling using single biopsies for patient treatment decision (Bettoni et al., 2017; Obeid et al., 2017). We show that a single biopsy accurately identifies low-infiltrated metastases, but the overall intra-metastatic immune infiltrate might be better estimated with multiple biopsies or sampling of larger tumor areas. Importantly, on biopsies, the performances of Immunoscore were superior to those of PDL1 in estimating the reality of the positivity across the whole metastatic slide. This illustrated the fact that PDL1 stainings were more heterogeneous in a given metastasis. Contrary to previous reports

Immunoscore (top: I0–2, black; I3–4, red) or TB score (bottom: TB0–2, black; TB34, red). Significant log rank p values are marked with as $^{**}0.005 \leq p < 0.01$, $^{*}0.01 \leq p < 0.05$.

(B) Forest plots showing the hazard ratio (HR) for DFS for immune markers, Immunoscore and TB score from the least-infiltrated metastasis per patient. Patient groups were defined based on high (Hi) or low (Lo) densities of each of the markers in the CT and IM. Cohort 1, optimal cutoff; cohort 2, optimal cutoff from cohort 1.

(C) Forest plots showing the HR for DFS for 3HS immune markers, Immunoscore and TB score. Within each cohort (1 and 2) the optimal cutoff in the least (Min)-infiltrated metastasis, over all metastases (Mean), highest (Max)-infiltrated metastasis, and randomly (Rand) selected metastasis from a patient was used.
See also Figure S7.

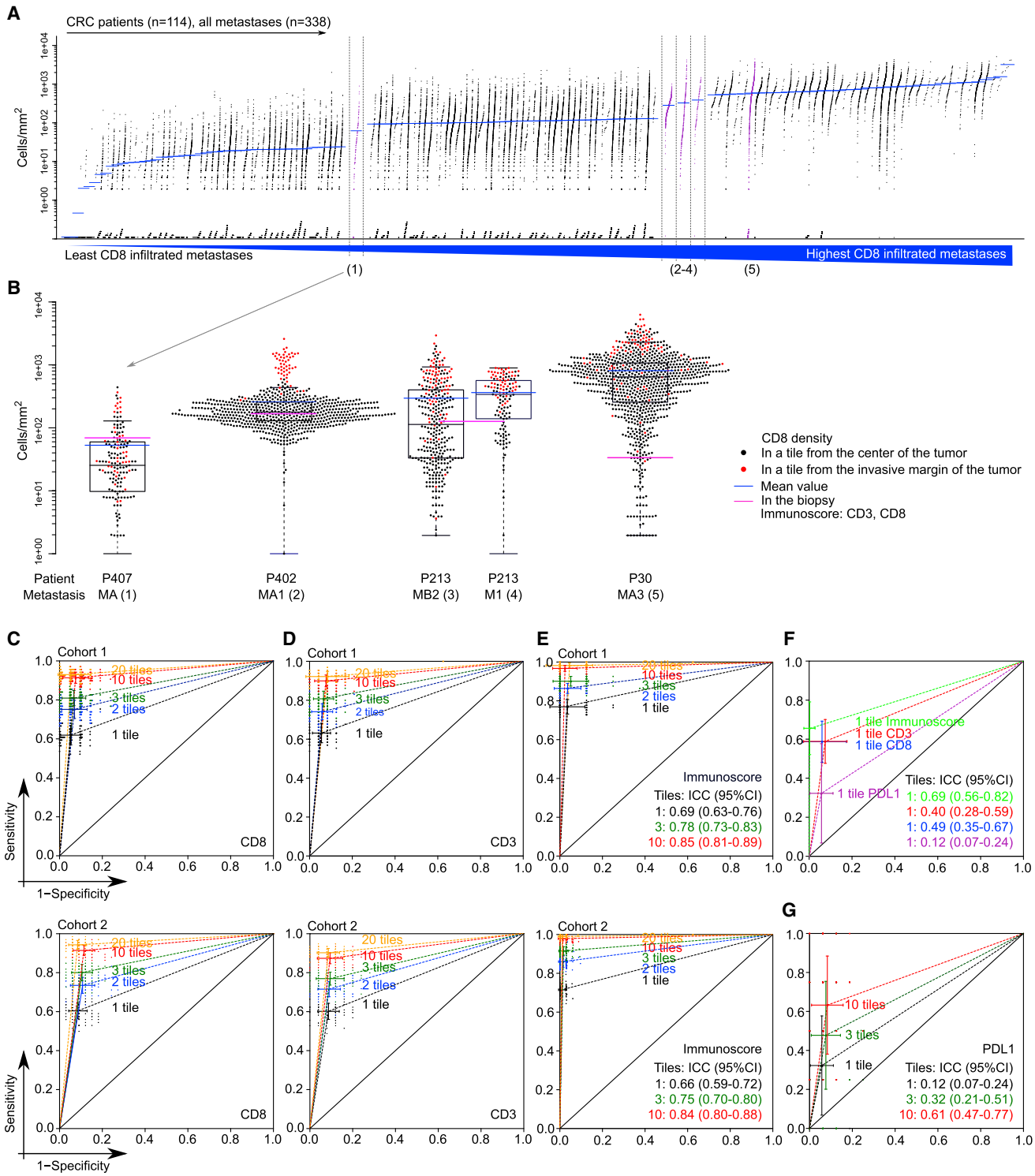

Figure 8. Immune Infiltrate of the Metastasis Estimated by Biopsies

(A) CD8 cytotoxic T cells measured in each of the tiles of the center of metastases (n = 338) from CRC patients (n = 114, cohort 1). Mean values of all tiles are indicated with a blue dash. Metastases were sorted based on mean CD8 densities from the lowest to intermediate and to the highest infiltrated metastasis, categories delimited by gray dashed vertical lines.

(B) CD8 density distribution plots are shown for five patients highlighted in (A). Each dot represents the CD8 density in one CT (black) or IM (red) tile of the analyzed metastasis. Mean values of all tiles (blue) and the CD8 density in the biopsy (pink). The boxplot in black shows the interquartile range (IQR) from the 25th to the 75th percentile, with the median line in the box and the whiskers at 1.5× IQR distance.

(legend continued on next page)

(Fadhil et al., 2012), a single tumor biopsy could thus limit and bias the discovery of biomarkers for targeted treatments.

A high Immunoscore was associated with a significantly lower number of metastases per patient. In particular, the patients with the fewest metastases had the highest immune intra-metastatic density in its least-infiltrated metastasis. CD3 and CD8 densities were higher in metastases compared with the primary tumors of the same patients showing no general loss of immunity within metastases. This could also reflect the development of an immunosuppressive microenvironment within the primary tumors over time, and this is supported by the higher FOXP3 densities observed within the CT of the primary tumors, particularly in anti-EGFR-treated patients. However, metastases from patients with highly infiltrated primary tumors also had higher densities of immune cells suggesting a more active systemic tumor-specific immune response.

Patients treated with chemotherapy and anti-EGFR had greater infiltration of T lymphocytes into the CT of metastases and higher Immunoscore than patients who received chemotherapy and anti-VEGF. Moreover we observed upregulation of B cell pathways (immune cell densities and gene expression) in primary tumors after anti-VEGF treatment.

The question remains, is the immune infiltrate a cause or consequence of tumor response to neoadjuvant treatment? Dying tumor cells could release antigen to further boost the tumor-specific immune response, similar to how a highly infiltrated metastasis may be poised for increased response. Phase 3 clinical trials have assessed the response to chemotherapy and anti-EGFR or anti-VEGF patients lacking *KRAS* mutations, with conflicting results (Heinemann et al., 2014; Primrose et al., 2014; Venook et al., 2017). Besides the expected effect on tumor cells, response to treatment may depend on a pre-existing immune response (Galon et al., 2013). Proinflammatory side effects, such as skin rash and increased EGFR-specific cytotoxic T lymphocyte frequency, during anti-EGFR treatment, suggests that EGFR may function as an immunogenic protein (Srivastava et al., 2013). EGFR pathway activation via mutation has been reported to promote an immunosuppressive microenvironment and treatment with EGFR tyrosine kinase inhibitors can downregulate PDL1 expression on tumor cells (Akbay et al., 2013). Anti-EGFR treatment may also drive natural killer cell-mediated antibody-dependent cell-mediated cytotoxicity via Fcγ receptors thus increasing dendritic cell priming (Hoffmann et al., 2009; Trivedi et al., 2015). Our results showing upregulated immune-related genes and increased adaptive immune cell infiltration in metastases from patients treated with anti-EGFR support these hypotheses.

Evaluation of immune infiltrate from biopsies could help to predict the response to preoperative radiochemotherapy of rectal cancer patients (Anitei et al., 2014). The T lymphocyte density and location in metastatic melanomas are reported to have predictive value for treatment outcome of patients receiving anti-PD1/PDL1 therapies (Tumeh et al., 2014). In these patients, a more clonal T cell population specifically correlates with response to PD1 blockade, but not CTLA4 (Roh et al., 2017). Our results suggest that, within metastatic CRCs, the adaptive immune response may play a role in preventing tumor recurrence. Despite evidence for immunoediting (Mlecnik et al., 2016a; Rooney et al., 2015), our data show the beneficial impact on prognosis of a T lymphocyte response throughout tumor invasion, including after the development of metastases. Cytotoxic T lymphocytes are positively associated with long-term survival of metastatic patients. The natural immunity and long-lasting capacity of memory T lymphocytes (Sallusto et al., 2004) could also play a central role for patient survival. Our data suggest that DFS and OS in stage IV patients are largely governed by the state of the local adaptive immune response within the metastases, in particular the least-infiltrated metastasis, representing the worst-case immune microenvironment, and therefore most likely site of tumor immune escape.

STAR★METHODS

Detailed methods are provided in the online version of this paper and include the following:

- KEY RESOURCES TABLE
- CONTACT FOR REAGENT AND RESOURCE SHARING
- EXPERIMENTAL MODEL AND SUBJECT DETAILS
  - Patients
- METHOD DETAILS
  - Immunohistochemistry Quantification, Analysis and Immunoscore
  - Analysis of Somatic Mutations
  - RAS and BRAF Mutations
  - Microsatellite Instability Status
- QUANTIFICATION AND STATISTICAL ANALYSIS
  - Statistical Analysis
- DATA AND SOFTWARE AVAILABILITY

SUPPLEMENTAL INFORMATION

Supplemental Information includes eight figures and three tables and can be found with this article online at https://doi.org/10.1016/j.ccell.2018.11.003.

ACKNOWLEDGMENTS

This work was supported by grants from the National Cancer Institute of France (INCa), the Canceropole Ile de France, the Plan Cancer, MedImmune,

(C–E) Receiver operating characteristics (ROC) were calculated for CD8 (C), CD3 (D), and Immunoscore (E) quantified in randomly selected CT tiles (100 times per patient). The specificity represents the likelihood of correctly predicting a low-biomarker biopsy when the metastasis is low, and the sensitivity represents the likelihood of correctly predicting a high-biomarker biopsy when the metastasis is high. The metastasis with the lowest CD8 infiltrate was analyzed for CD8 (C), CD3 (D), and Immunoscore (E) in cohort 1 (top, n = 114 patients) and cohort 2 (bottom, n = 108 patients). Patients were sorted based on immune densities of each marker from either, 1 (black), 2 (blue), 3 (green), 10 (red), and 20 (orange) tiles and high or low patient groups were defined using the optimal cutoff of the marker at cohort level. The classification of patients based on random tiles was further compared with the whole-slide immune density classification.
(F and G) ROC for Immunoscore (green), CD3 (red), CD8 (blue), and PDL1 (purple) with one tile (F) and for PDL1 with 1 (black), 3 (green), 10 (red) tiles (G) calculated as in (C–E). The 1% stained tile surface cutoff (~19 cells) was applied for PDL1 (n = 20 patients). The concordance among the 100 random biopsy repetitions for the different tile numbers was estimated using the intraclass correlation (ICC).
See also Figure S8.

INSERM, the Cancer Research for Personalized Medicine (CARPEM), Paris Alliance of Cancer Research Institutes (PACRI). This work was supported by the European Union's Horizon 2020 research and innovation program under grant agreement no. 633592 "APERIM: Advanced Bioinformatics Tools for Personalized Cancer Immunotherapy," by ERAnet Transcan grant "Integrative cancer-immunology and Immunoscore for cancer classification and immunotherapies," by the LabEx Immuno-oncology, the Fondation St-Luc and the CPTCR (Cliniques des Pathologies Tumorales du Colon et du Rectum) of the Cliniques Universitaires St-Luc. We thank Erwan Morgand, Géraldine Pairet, Javier Carrasco, and Yves Humblet for their important contributions.

AUTHOR CONTRIBUTIONS

Study Concept and Design, J.G., M.V.d.E., B.M., and G.B..; Acquisition of Data, M.V.d.E., S.E.C., A.V., T.F., L.F., N.H., and F.M.; Analysis and Interpretation of Data, B.M., M.V.d.E., G.B., and J.G.; Drafting of the Manuscript, J.G., B.M., M.V.D.E., and G.B.; Critical Revision of the Manuscript, J.G., B.M., M.V.d.E., G.B., F.P., J.-P.M., V.V.-A., M.A., D.B., A.J.-M., P.B., K.H., E.V.C., A.K., C.R., and D.L.; Statistical Analysis, B.M. and G.B.; Obtained Funding, J.G., M.V.d.E., F.P., and J.-P.M.; Technical Support, S.E.C., A.V., T.F., L.F., N.H., A.D., and F.M.; Material Support, M.V.d.E., N.H., A.D., G.P., J.-F.G., C.H., and F.P.; Study Supervision, J.G.

DECLARATION OF INTERESTS

Immunoscore is a registered trademark from INSERM. J.G. is co-founder and chairman of the scientific advisory board of HalioDx. J.G., B.M., and F.P. have patents associated with "*in vitro* method for the prognosis of progression of a cancer" (PCT/IB2006/003168, PCT/EP2013/062405).

Received: December 20, 2017
Revised: September 11, 2018
Accepted: November 5, 2018
Published: December 10, 2018

REFERENCES

Akbay, E.A., Koyama, S., Carretero, J., Altabef, A., Tchaicha, J.H., Christensen, C.L., Mikse, O.R., Cherniack, A.D., Beauchamp, E.M., Pugh, T.J., et al. (2013). Activation of the PD-1 pathway contributes to immune escape in EGFR-driven lung tumors. Cancer Discov. *3*, 1355–1363.

Alizadeh, A.A., Aranda, V., Bardelli, A., Blanpain, C., Bock, C., Borowski, C., Caldas, C., Califano, A., Doherty, M., Elsner, M., et al. (2015). Toward understanding and exploiting tumor heterogeneity. Nat. Med. *21*, 846–853.

Allegra, C.J., Rumble, R.B., Hamilton, S.R., Mangu, P.B., Roach, N., Hantel, A., and Schilsky, R.L. (2016). Extended RAS gene mutation testing in metastatic colorectal carcinoma to predict response to anti-epidermal growth factor receptor monoclonal antibody therapy: American Society of Clinical Oncology Provisional Clinical Opinion Update 2015. J. Clin. Oncol. *34*, 179–185.

Angelova, M., Mlecnik, B., Vasaturo, A., Bindea, G., Fredriksen, T., Lafontaine, L., Buttard, B., Morgand, E., Bruni, D., Jouret-Mourin, A., et al. (2018). Evolution of metastases in space and time under immune selection. Cell *175*, 751–765.e16.

Anitei, M.G., Zeitoun, G., Mlecnik, B., Marliot, F., Haicheur, N., Todosi, A.M., Kirilovsky, A., Lagorce, C., Bindea, G., Ferariu, D., et al. (2014). Prognostic and predictive values of the immunoscore in patients with rectal cancer. Clin. Cancer Res. *20*, 1891–1899.

Berghoff, A.S., Fuchs, E., Ricken, G., Mlecnik, B., Bindea, G., Spanberger, T., Hackl, M., Widhalm, G., Dieckmann, K., Prayer, D., et al. (2016). Density of tumor-infiltrating lymphocytes correlates with extent of brain edema and overall survival time in patients with brain metastases. Oncoimmunology *5*, e1057388.

Bettoni, F., Masotti, C., Habr-Gama, A., Correa, B.R., Gama-Rodrigues, J., Vianna, M.R., Vailati, B.B., Sao Juliao, G.P., Fernandez, L.M., Galante, P.A., et al. (2017). Intratumoral genetic heterogeneity in rectal cancer: are single biopsies representative of the entirety of the tumor? Ann. Surg. *265*, e4–e6.

Bindea, G., Galon, J., and Mlecnik, B. (2013a). CluePedia Cytoscape plugin: pathway insights using integrated experimental and in silico data. Bioinformatics *29*, 661–663.

Bindea, G., Mlecnik, B., Fridman, W.H., Pages, F., and Galon, J. (2010). Natural immunity to cancer in humans. Curr. Opin. Immunol. *22*, 215–222.

Bindea, G., Mlecnik, B., Hackl, H., Charoentong, P., Tosolini, M., Kirilovsky, A., Fridman, W.H., Pages, F., Trajanoski, Z., and Galon, J. (2009). ClueGO: a Cytoscape plug-in to decipher functionally grouped gene ontology and pathway annotation networks. Bioinformatics *25*, 1091–1093.

Bindea, G., Mlecnik, B., Tosolini, M., Kirilovsky, A., Waldner, M., Obenauf, A.C., Angell, H., Fredriksen, T., Lafontaine, L., Berger, A., et al. (2013b). Spatiotemporal dynamics of intratumoral immune cells reveal the immune landscape in human cancer. Immunity *39*, 782–795.

Debucquoy, A., Haustermans, K., Daemen, A., Aydin, S., Libbrecht, L., Gevaert, O., De Moor, B., Tejpar, S., McBride, W.H., Penninckx, F., et al. (2009). Molecular response to cetuximab and efficacy of preoperative cetuximab-based chemoradiation in rectal cancer. J. Clin. Oncol. *27*, 2751–2757.

Edelbauer, M., Datta, D., Vos, I.H., Basu, A., Stack, M.P., Reinders, M.E., Sho, M., Calzadilla, K., Ganz, P., and Briscoe, D.M. (2010). Effect of vascular endothelial growth factor and its receptor KDR on the transendothelial migration and local trafficking of human T cells in vitro and in vivo. Blood *116*, 1980–1989.

Fadhil, W., Ibrahem, S., Seth, R., AbuAli, G., Ragunath, K., Kaye, P., and Ilyas, M. (2012). The utility of diagnostic biopsy specimens for predictive molecular testing in colorectal cancer. Histopathology *61*, 1117–1124.

Fridman, W.H., Pages, F., Sautes-Fridman, C., and Galon, J. (2012). The immune contexture in human tumours: impact on clinical outcome. Nat. Rev. Cancer *12*, 298–306.

Galon, J., Angell, H.K., Bedognetti, D., and Marincola, F.M. (2013). The continuum of cancer immunosurveillance: prognostic, predictive, and mechanistic signatures. Immunity *39*, 11–26.

Galon, J., Costes, A., Sanchez-Cabo, F., Kirilovsky, A., Mlecnik, B., Lagorce-Pagès, C., Tosolini, M., Camus, M., Berger, A., Wind, P., et al. (2006). Type, density, and location of immune cells within human colorectal tumors predict clinical outcome. Science *313*, 1960–1964.

Galon, J., Mlecnik, B., Bindea, G., Angell, H.K., Berger, A., Lagorce, C., Lugli, A., Zlobec, I., Hartmann, A., Bifulco, C., et al. (2014). Towards the introduction of the 'Immunoscore' in the classification of malignant tumours. J. Pathol. *232*, 199–209.

Galon, J., Pages, F., Marincola, F.M., Thurin, M., Trinchieri, G., Fox, B.A., Gajewski, T.F., and Ascierto, P.A. (2012). The immune score as a new possible approach for the classification of cancer. J. Transl. Med. *10*, 1.

Gerlinger, M., Rowan, A.J., Horswell, S., Larkin, J., Endesfelder, D., Gronroos, E., Martinez, P., Matthews, N., Stewart, A., Tarpey, P., et al. (2012). Intratumor heterogeneity and branched evolution revealed by multiregion sequencing. N. Engl. J. Med. *366*, 883–892.

Halama, N., Michel, S., Kloor, M., Zoernig, I., Benner, A., Spille, A., Pommerencke, T., von Knebel, D.M., Folprecht, G., Luber, B., et al. (2011). Localization and density of immune cells in the invasive margin of human colorectal cancer liver metastases are prognostic for response to chemotherapy. Cancer Res. *71*, 5670–5677.

Heinemann, V., von Weikersthal, L.F., Decker, T., Kiani, A., Vehling-Kaiser, U., Al-Batran, S.E., Heintges, T., Lerchenmuller, C., Kahl, C., Seipelt, G., et al. (2014). FOLFIRI plus cetuximab versus FOLFIRI plus bevacizumab as first-line treatment for patients with metastatic colorectal cancer (FIRE-3): a randomised, open-label, phase 3 trial. Lancet Oncol. *15*, 1065–1075.

Hoffmann, T.K., Schirlau, K., Sonkoly, E., Brandau, S., Lang, S., Pivarcsi, A., Balz, V., Muller, A., Homey, B., Boelke, E., et al. (2009). A novel mechanism for anti-EGFR antibody action involves chemokine-mediated leukocyte infiltration. Int. J. Cancer *124*, 2589–2596.

Jemal, A., Siegel, R., Ward, E., Hao, Y., Xu, J., Murray, T., and Thun, M.J. (2008). Cancer statistics, 2008. CA Cancer J. Clin. *58*, 71–96.

Katz, S.C., Bamboat, Z.M., Maker, A.V., Shia, J., Pillarisetty, V.G., Yopp, A.C., Hedvat, C.V., Gonen, M., Jarnagin, W.R., Fong, Y., et al. (2013). Regulatory

T cell infiltration predicts outcome following resection of colorectal cancer liver metastases. Ann. Surg. Oncol. *20*, 946–955.

Kwak, Y., Koh, J., Kim, D.W., Kang, S.B., Kim, W.H., and Lee, H.S. (2016). Immunoscore encompassing CD3+ and CD8+ T cell densities in distant metastasis is a robust prognostic marker for advanced colorectal cancer. Oncotarget *7*, 81778–81790.

Langley, R.R., and Fidler, I.J. (2007). Tumor cell-organ microenvironment interactions in the pathogenesis of cancer metastasis. Endocr. Rev. *28*, 297–321.

Manceau, G., Marisa, L., Boige, V., Duval, A., Gaub, M.P., Milano, G., Selves, J., Olschwang, S., Jooste, V., le Legrain, M., et al. (2015). PIK3CA mutations predict recurrence in localized microsatellite stable colon cancer. Cancer Med. *4*, 371–382.

Mlecnik, B., Bindea, G., Angell, H.K., Maby, P., Angelova, M., Tougeron, D., Church, S.E., Lafontaine, L., Fischer, M., Fredriksen, T., et al. (2016a). Integrative analyses of colorectal cancer show immunoscore is a stronger predictor of patient survival than microsatellite instability. Immunity *44*, 698–711.

Mlecnik, B., Bindea, G., Angell, H.K., Sasso, M.S., Obenauf, A.C., Fredriksen, T., Lafontaine, L., Bilocq, A.M., Kirilovsky, A., Tosolini, M., et al. (2014). Functional network pipeline reveals genetic determinants associated with in situ lymphocyte proliferation and survival of cancer patients. Sci. Transl. Med. *6*, 228ra237.

Mlecnik, B., Bindea, G., Kirilovsky, A., Angell, H.K., Obenauf, A.C., Tosolini, M., Church, S.E., Maby, P., Vasaturo, A., Angelova, M., et al. (2016b). The tumor microenvironment and Immunoscore are critical determinants of dissemination to distant metastasis. Sci. Transl. Med. *8*, 327ra326.

Mlecnik, B., Tosolini, M., Kirilovsky, A., Berger, A., Bindea, G., Meatchi, T., Bruneval, P., Trajanoski, Z., Fridman, W.H., Pages, F., et al. (2011). Histopathologic-based prognostic factors of colorectal cancers are associated with the state of the local immune reaction. J. Clin. Oncol. *29*, 610–618.

Mlecnik, B., Van den Eynde, M., Bindea, G., Church, S.E., Vasaturo, A., Fredriksen, T., Lafontaine, L., Haicheur, N., Marliot, F., Debetancourt, D., et al. (2018). Comprehensive intrametastatic immune quantification and major impact of immunoscore on survival. J. Natl. Cancer Inst. *110*, https://doi.org/10.1093/jnci/djx123.

Nosho, K., Baba, Y., Tanaka, N., Shima, K., Hayashi, M., Meyerhardt, J.A., Giovannucci, E., Dranoff, G., Fuchs, C.S., and Ogino, S. (2010). Tumour-infiltrating T-cell subsets, molecular changes in colorectal cancer, and prognosis: cohort study and literature review. J. Pathol. *222*, 350–366.

Obeid, J.M., Hu, Y., Erdag, G., Leick, K.M., and Slingluff, C.L., Jr. (2017). The heterogeneity of tumor-infiltrating CD8+ T cells in metastatic melanoma distorts their quantification: how to manage heterogeneity? Melanoma Res. *27*, 211–217.

Okano, K., Maeba, T., Moroguchi, A., Ishimura, K., Karasawa, Y., Izuishi, K., Goda, F., Usuki, H., Wakabayashi, H., and Maeta, H. (2003). Lymphocytic infiltration surrounding liver metastases from colorectal cancer. J. Surg. Oncol. *82*, 28–33.

Pages, F., Berger, A., Camus, M., Sanchez-Cabo, F., Costes, A., Molidor, R., Mlecnik, B., Kirilovsky, A., Nilsson, M., Damotte, D., et al. (2005). Effector memory T cells, early metastasis, and survival in colorectal cancer. N. Engl. J. Med. *353*, 2654–2666.

Pages, F., Kirilovsky, A., Mlecnik, B., Asslaber, M., Tosolini, M., Bindea, G., Lagorce, C., Wind, P., Marliot, F., Bruneval, P., et al. (2009). In situ cytotoxic and memory T cells predict outcome in patients with early-stage colorectal cancer. J. Clin. Oncol. *27*, 5944–5951.

Pages, F., Mlecnik, B., Marliot, F., Bindea, G., Ou, F.S., Bifulco, C., Lugli, A., Zlobec, I., Rau, T.T., Berger, M.D., et al. (2018). International validation of the consensus Immunoscore for the classification of colon cancer: a prognostic and accuracy study. Lancet *391*, 2128–2139.

Prendergast, G.C., and Jaffee, E.M. (2007). Cancer immunologists and cancer biologists: why we didn't talk then but need to now. Cancer Res. *67*, 3500–3504.

Primrose, J., Falk, S., Finch-Jones, M., Valle, J., O'Reilly, D., Siriwardena, A., Hornbuckle, J., Peterson, M., Rees, M., Iveson, T., et al. (2014). Systemic chemotherapy with or without cetuximab in patients with resectable colorectal liver metastasis: the New EPOC randomised controlled trial. Lancet Oncol. *15*, 601–611.

Pugh, S.A., Harrison, R.J., Primrose, J.N., and Khakoo, S.I. (2014). T cells but not NK cells are associated with a favourable outcome for resected colorectal liver metastases. BMC Cancer *14*, 180.

Roh, W., Chen, P.L., Reuben, A., Spencer, C.N., Prieto, P.A., Miller, J.P., Gopalakrishnan, V., Wang, F., Cooper, Z.A., Reddy, S.M., et al. (2017). Integrated molecular analysis of tumor biopsies on sequential CTLA-4 and PD-1 blockade reveals markers of response and resistance. Sci. Transl. Med. *9*, https://doi.org/10.1126/scitranslmed.aah3560.

Rooney, M.S., Shukla, S.A., Wu, C.J., Getz, G., and Hacohen, N. (2015). Molecular and genetic properties of tumors associated with local immune cytolytic activity. Cell *160*, 48–61.

Sallusto, F., Geginat, J., and Lanzavecchia, A. (2004). Central memory and effector memory T cell subsets: function, generation, and maintenance. Annu. Rev. Immunol. *22*, 745–763.

Silva, I.P., Salhi, A., Giles, K.M., Vogelsang, M., Han, S.W., Ismaili, N., Lui, K.P., Robinson, E.M., Wilson, M.A., Shapiro, R.L., et al. (2016). Identification of a novel pathogenic germline KDR variant in melanoma. Clin. Cancer Res. *22*, 2377–2385.

Srivastava, R.M., Lee, S.C., Andrade Filho, P.A., Lord, C.A., Jie, H.B., Davidson, H.C., Lopez-Albaitero, A., Gibson, S.P., Gooding, W.E., Ferrone, S., et al. (2013). Cetuximab-activated natural killer and dendritic cells collaborate to trigger tumor antigen-specific T-cell immunity in head and neck cancer patients. Clin. Cancer Res. *19*, 1858–1872.

Tanis, E., Julie, C., Emile, J.F., Mauer, M., Nordlinger, B., Aust, D., Roth, A., Lutz, M.P., Gruenberger, T., Wrba, F., et al. (2015). Prognostic impact of immune response in resectable colorectal liver metastases treated by surgery alone or surgery with perioperative FOLFOX in the randomised EORTC study 40983. Eur. J. Cancer *51*, 2708–2717.

Trivedi, S., Concha-Benavente, F., Srivastava, R.M., Jie, H.B., Gibson, S.P., Schmitt, N.C., and Ferris, R.L. (2015). Immune biomarkers of anti-EGFR monoclonal antibody therapy. Ann. Oncol. *26*, 40–47.

Tumeh, P.C., Harview, C.L., Yearley, J.H., Shintaku, I.P., Taylor, E.J., Robert, L., Chmielowski, B., Spasic, M., Henry, G., Ciobanu, V., et al. (2014). PD-1 blockade induces responses by inhibiting adaptive immune resistance. Nature *515*, 568–571.

Venook, A.P., Niedzwiecki, D., Lenz, H.J., Innocenti, F., Fruth, B., Meyerhardt, J.A., Schrag, D., Greene, C., O'Neil, B.H., Atkins, J.N., et al. (2017). Effect of first-line chemotherapy combined with cetuximab or bevacizumab on overall survival in patients with KRAS wild-type advanced or metastatic colorectal cancer: a Randomized Clinical Trial. JAMA *317*, 2392–2401.

Verstraete, M., Debucquoy, A., Dekervel, J., van Pelt, J., Verslype, C., Devos, E., Chiritescu, G., Dumon, K., D'Hoore, A., Gevaert, O., et al. (2015). Combining bevacizumab and chemoradiation in rectal cancer. Translational results of the AXEBeam trial. Br. J. Cancer *112*, 1314–1325.

Wang, E., Panelli, M.C., Monsurro, V., and Marincola, F.M. (2004). A global approach to tumor immunology. Cell. Mol. Immunol. *1*, 256–265.

Zhang, J., Fujimoto, J., Zhang, J., Wedge, D.C., Song, X., Zhang, J., Seth, S., Chow, C.W., Cao, Y., Gumbs, C., et al. (2014). Intratumor heterogeneity in localized lung adenocarcinomas delineated by multiregion sequencing. Science *346*, 256–259.

Ziv, E., Bergen, M., Yarmohammadi, H., Boas, F.E., Petre, E.N., Sofocleous, C.T., Yaeger, R., Solit, D.B., Solomon, S.B., and Erinjeri, J.P. (2017). PI3K pathway mutations are associated with longer time to local progression after radioembolization of colorectal liver metastases. Oncotarget *8*, 23529–23538.

STAR★METHODS

KEY RESOURCES TABLE

REAGENT or RESOURCE	SOURCE	IDENTIFIER
Antibodies		
Rabbit monoclonal anti-CD3 (IHC)	Roche, Ventana	RRID: AB_2335978; clone 2GV6
Mouse monoclonal anti-CD8 (IHC)	Dako	RRID: AB_2075537; clone 4B11
Mouse monoclonal anti-CD20 (IHC)	Dako	RRID: AB_233595; clone L26
Mouse monoclonal anti-CD45RO (IHC)	Dako	Cat#M074201-2; clone UCHL1
Mouse monoclonal anti-FOXP3 (IHC)	AbCam	RRID: AB_445284; clone 236A/E7
Mouse monoclonal anti-CD68 (IHC)	Thermofisher	RRID: AB_10979558; clone PGM1
Mouse monoclonal anti-CTLA4 (IHC)	R&D Systems	RRID: AB_2276879; clone 48815
Mouse monoclonal anti-PD1 (IHC)	Ventana	Cat#760-4895, clone NAT105
Mouse monoclonal anti-PDL1 (IHC)	Cell Signaling Technologies	RRID: AB_2687655; clone E1L3N
Biological Samples		
Primary colorectal tumors	Cliniques Universitaires St-Luc, Belgium	Cohort 1 and 2
Lung metastases of colorectal cancer	Cliniques Universitaires St-Luc, Belgium	Cohort 1
Liver metastases of colorectal cancer	Cliniques Universitaires St-Luc, Belgium	Cohort 1 and 2
Critical Commercial Assays		
FFPE Plus LEV DNA purification kit	Promega	
DAKO EnVision+ HRP polymer and DAB detection	Dako	
Ultraview Universal DAB Detection kit,	Ventana	Cat#760-500
Ion AmpliSeq™ Cancer Hotspot Panel v2	IonTorrent, Life Technologies	Cat# 4475346
Deposited Data		
Rectal cancer data	GEO: GSE60331	cohort 3, 4
Software and Algorithms		
Alamut (v2.4.1)	Interactive Biosoftware	www.interactive-biosoftware.com/alamut-visual/
R (v3.2.3)	The R Project for Statistical Computing	www.r-project.org
Genesis (v1.7.7)	Genesis Software	genome.tugraz.at/genesisclient
ClueGO (v2.5.1)	ClueGO software	apps.cytoscape.org/apps/cluego
CluePedia (v1.5.1)	CluePedia software	apps.cytoscape.org/apps/cluepedia
Cytoscape (v3.6.1)	Cytoscape software	www.cytoscape.org
Immunoscore software	HalioDx, Definiens	Haliodx.com

CONTACT FOR REAGENT AND RESOURCE SHARING

Further information and requests for resources and reagents should be directed to and will be fulfilled by the Lead Contact, Jérôme Galon (jerome.galon@crc.jussieu.fr).

EXPERIMENTAL MODEL AND SUBJECT DETAILS

Patients

All detailed patient related information for cohorts 1 and 2 can be found in Tables S1 and S2. Cohorts 3 and 4 are 56 locally advanced rectal cancer patients previously described ((Debucquoy et al., 2009; Verstraete et al., 2015)).

All synchronous or metachronous colorectal metastases from 114 patients (cohort 1, 338 metastases) and 108 patients (cohort 2, validation, 265 metastases) who underwent curative resection with or without preoperative treatment at the Cliniques Universitaires St-Luc between 2004 and 2017 were analyzed (Tables S2 and S3; cohort 1 and 2). Additionally, 97 corresponding primary CRC tumors were available for analysis. The formalin-fixed paraffin embedded tissues of all resected metastases (and primary tumor when possible) must be available for inclusion in the study. The patient clinical characteristics and the type of preoperative treatment

(chemotherapy alone, chemotherapy + anti-VEGF, chemotherapy + anti-EGFR or none) were monitored. The observation period was the interval between curative surgery of CRC metastases and the last contact (death or final follow-up). Data were censored according to the final follow-up for patients who had not relapsed or died. The mean duration of the follow-up was 44.5 months. Chemotherapy regimens were oxaliplatin or irinotecan + fluoropyrimidine; anti-VEGF and anti-EGFR treatments were mainly bevacizumab and cetuximab respectively (monoclonal antibodies). The presence of *RAS* and *BRAF* mutations and MSI status were assessed for all patients. A secure, Web-based database was assembled to integrate clinical data sets and the results of whole-slide immunochemistry quantification. Approval for this research including cohorts 1 and 2 was obtained from the ethics committees of the Cliniques Universitaires St-Luc, and the informed consent was obtained from the patients.

Additionally, 56 locally advanced rectal cancer patients included in 2 prospective trials (Debucquoy et al., 2009; Verstraete et al., 2015) with available tumor gene expression analysis (Affymetrix) before and after one single perfusion of anti-VEGF (bevacizumab) (n=16; cohort 3, Gene Expression Omnibus: GSE60331, (Verstraete et al., 2015)) or anti-EGFR (cetuximab) (n=40; cohort 4, (Debucquoy et al., 2009)) were included for analysis. The translational and clinical parts of studies involving cohorts 3 (Verstraete et al., 2015) and 4 (Debucquoy et al., 2009) were approved by the Independent Ethics Committee and Belgian Health authority, and the informed consent was obtained from the patients.

METHOD DETAILS

Immunohistochemistry Quantification, Analysis and Immunoscore

Immunohistochemistry was performed on 5 μM sections of formalin-fixed paraffin embedded (FFPE) tissues from resected metastases and primary tumors. Automated staining was performed on either a Ventana Benchmark or Discovery XT (Roche) for CD3 (2GV6, Ventana), CD8 (4B11, Dako), CD45RO (UCHL1, DAKO), CD20 (L29, DAKO), FOXP3 (236A/E7, Abcam), CD68 (PG-M1, Dako), CTLA-4 (R&D Systems) and PD1 (NAT105, Ventana) using the ultraView Universal DAB IHC Detection Kit or ChromoMap DAB kit, respectively (Ventana). NKp46 (195314, R&D Systems) and PDL1 (EIL3N, Cell Signaling Technologies) detection was performed manually. Manually stained slides were hydrated, subject to antigen retrieval, 1 hour or overnight monoclonal antibody incubation, followed by secondary detection using the species-specific DAKO EnVision+ HRP polymer and DAB detection (Dako). All slides were scanned using a Hamamatsu NanoZoomer at 20x magnification. Definition of the CT and IM for each slide and expression of immune markers was digitally quantified using Definiens Developer XD. For each image a grid of tiles covering the CT and IM of the tumor tissue were analyzed for the immune density (cells/mm^2) measured as global infiltration (whole metastasis slide) or as 3 hot-spots (3HS) of the most highly infiltrated tiles for each the CT and IM. Both whole slide and 3 hot-spot (3HS) analyses were used to calculate the CD3/CD8 Immunoscore (I) (Galon et al., 2012; Galon et al., 2014). Briefly, Immunoscore ranging from 0 (I0), when low densities of two cell types are found in both regions, to 4 (I4), when high densities are found of two cell types in both regions. The Immunoscore was calculated using the mean of 3HS or the whole slide information per region.

Analysis of Somatic Mutations

Genomic DNA from 56 CRC metastases (lung and liver) and 8 primary tumors of 12 patients showing the highest intermetastatic immune heterogeneity was extracted from two 5 μm thick FFPE slides using Maxwell 16 FFPE Plus LEV DNA purification kit (Promega). The quantity of DNA was determined using Qubit 2.0 fluorometer (Invitrogen, life Technologies) and 20 ng of extracted DNA was amplified using the Ion AmpliSeq Cancer HotSpot Panel V2 (Life Technologies) according to the manufacturer's protocol. Briefly, commonly mutated exons from 50 oncogenes or tumor suppressor genes (Table S1) were amplified using a panel of 207 primer pairs in a 20-cycle PCR reaction. Subsequently amplicons were digested with FuPa reagent and samples were separately barcoded with Ion Xpress barcodes. IonAmpliSeq adapters were then added to each sample. DNA banks were purified using Agencourt AMPure XP reagent (Beckman Coulter) and purified libraries were amplified using Platinum PCR supermix high fidelity enzyme and purified again with Agencourt according to the manufacturer's instructions (Ion AmpliSeq Library kit 2.0, ion torrent, Life Technologies). The quality and quantity of each library was evaluated by High Sensitivity DNA chip (Agilent Technologies). Patients were then mixed and libraries obtained were amplified and enriched using the ion OneTouch 2 system (Ion PGM Template OT2 200, Life technologies). Sequencing was performed with the Ion Torrent PGM system using Ion316 chip and the Ion PGM sequencing 200 kit V2 in a 520 cycle run. Data were aligned using Variant Caller (V4.2.1.0) plugin compared to Hg19 database and results were analysed using Alamut 2.4.1 software (Interactive Biosoftware).

RAS and BRAF Mutations

Genomic DNA from Primary Tumor and, if not available, corresponding metastasis was extracted and purified from two 5um thick FFPE slides using a NucleoSpin® Tissue Kit (Macherey-Nagel, Düren, Germany) according to the manufacturer's recommendations. DNA quantity was determined by NanoDrop spectrophotometry (NanoDrop Technologies, Wilmington, DE, USA). A screening genotyping for selected polymorphisms in *KRAS* (exon 2: codon 12 and 13) and *BRAF* (exon 15, codon 600) was performed by PCR followed by pyrosequencing on the PyroMark Q96ID Sequencer (Qiagen, Hilden, Germany) according to the manufacturer's protocol. Each pyro-sequencing run included a negative control. Other *RAS* mutation including *KRAS* exon 3 (codons 59 and 61) and exon 4 (codons 117 and 146) and *NRAS* (exon 2: codons 12 and 13; exon 3: codons 59 and 61; exon 4: codons 117 and 146) were evaluated by a similar technique only for patients with *KRAS* (exon 2) wild-type (wt) and *BRAF* wt. The frequency of *RAS* gene mutations was assessed, and the distribution of codons that were affected and the specific nucleotide substitution of each assay were determined.

A cutoff of 10% of alleles mutated in each reaction defined a mutated case. Based on their mutational status and considering the fact that *RAS* and *BRAF* mutation are mutually exclusive, patients were categorized as: *BRAF* wt or mutated and *RAS* (*KRAS* exon 2,3 and 4 and *NRAS* exon 2, 3 and 4) wt or mutated.

Microsatellite Instability Status

Sections (5 μm) from each paraffin block from primary tumor and, if not available, the corresponding metastasis were routinely immunostained on Benchmark XT automate from Ventana (Tucson, AZ, USA). Except for the primary antibody anti-PMS2 (clone EPR-3947, ready to use from Ventana), antibodies anti-MLH1 (clone G168-15, BD Biosciences), anti-MSH2 (clone G219-1129, BD Biosciences) and anti-MSH6 (clone 44, Transduction Laboratories) were diluted with the antibody diluent solution (ref.251-018, Ventana) at 1/30, 1/200 and 1/50 respectively. Specific antibody labelling was visualized using DAB-peroxidase UltraView Universal detection Kit (ref. 760-500; Ventana) according to the vendor's protocol. Normal colonic epithelial and stromal cells served as internal positive controls. Tumours showing loss or significantly reduced expression of any mismatch repair proteins (MMR), compared with positive controls, were deemed to be MMR-deficient tumour (MSI tumour), whereas those retaining all four MMR proteins were MMR-intact tumour (MSS tumour).

In addition, microsatellite instability status was assessed using the classical molecular new Bethesda panel (BAT25, BAT26, NR21, NR24, NR27) in each of the metastases.

QUANTIFICATION AND STATISTICAL ANALYSIS

Statistical Analysis

All confidence intervals shown on the bar plots are based on ±SEM. T-test and Wilcoxon–Mann–Whitney tests were applied to identify immune markers reaching a significant difference in density levels among clinical parameters. Fisher's exact test was used to assess the over-representation of immune parameters in clinical groups.

To account for the dependency among multiple metastases from the same patient, analyses on the metastasis level are based on a multi level model approach by using a linear mixed-effects (lme) model fit by REML for testing categorical vs. numeric data from the 'nlme' R package.

Affymetrix experiments were performed as previously described (Verstraete et al., 2015). Expression data was normalized using the RMA method using R and the Immune cell densities were visualized in Genesis. Gene expression data was analyzed with ClueGO v2.5.2 (Bindea et al., 2009) and CluePedia v1.5.2 (Bindea et al., 2013a) Cytoscape v3.6.1 apps and was based on Gene Ontology, KEGG, Reactome and WikiPathway.

Kaplan–Meier curves were used to assess the impact of pre-operative treatment and Immunoscore on overall (OS) and disease-free survival (DFS). The significance of clinical characteristics was determined by univariate analysis using the log-rank test and Cox proportional hazards models. Immune cell markers were dichotomized using the minimal P-value approach and all obtained cutoffs from the test cohort 1 were validated on the validation cohort 2.

The intraclass correlation (ICC) was estimated using ICC R package.

All analyses were performed using R (3.2.3), (survival, Hmisc, forestplot and ICC packages).

All tests were two-sided and a p-value of less than 0.05 was considered statistically significant.

DATA AND SOFTWARE AVAILABILITY

Gene expression (Affymetrix) data for locally advanced rectal cancer patients (Verstraete et al., 2015) are available in GEO (GSE60331).